Evaluating Sentinel-1 Volume Scattering based Snow Depth Retrievals over NASA SnowEx Sites

Zachary Hoppinen[1, 2], Ross Palomaki[3, 4], George Brencher[5], Devon Dunmire[6,7], Eric Gagliano[5], Adrian Marziliano[8], Naheem Adebisi[1], Jack Tarricone[9,10], Randall Bonnell[11], and Hans-Peter Marshall[1]

[1]Boise State University, Department of Geosciences, 1295 University Drive, Boise, ID, USA
[2]Cold Regions Research and Engineering Laboratory, Engineer Research and Development Center, United States Army, Hanover, NH 03755, USA
[3]Institute of Arctic and Alpine Research, University of Colorado, 4001 Discovery Dr, Boulder, CO 80303
[4]Department of Earth Sciences, Montana State University, Bozeman, Montana, USA
[5]Civil and Environmental Engineering Department, University of Washington, Seattle, WA 98195 USA
[6]Department of Earth and Environmental Sciences, KU Leuven, Heverlee, Belgium
[7]Department of Atmospheric and Oceanic Sciences, CU Boulder, 4001 Discovery Dr, Boulder, CO 80303
[8]Center for Water and the Environment, University of New Mexico, Albuquerque, NM 87131, USA
[9]Hydrological Sciences Laboratory, NASA Goddard Space Flight Center, Greenbelt, MD 20770, USA
[10]NASA Postdoctoral Program, NASA Goddard Space Flight Center, Greenbelt, MD 20770, USA
[11]Department of Geosciences, Colorado State University, Fort Collins, CO 80523, USA

Correspondence: Zachary Hoppinen (Zachary.Hoppinen@u.boisestate.edu)

Abstract. The Sentinel-1 satellite has been used to retrieve snow depth estimates based on the volume scattering of C-band microwave radar within the snowpack. This study evaluates a Sentinel-1 C-band snow depth retrieval algorithm against nine high-resolution lidar snow depth acquisitions collected during the winters of 2019-2020 and 2020–21 at six study sites across the western United States. We first evaluate the relationship between the Sentinel-1 cross ratio (VH /VV) backscatter and find significant relationships between measured snow depths and cumulative changes in the cross ratio for snow depths above 1.5 m. At 90 m resolution, comparisons between lidar and Sentinel-1 snow depth retrievals show moderate correlations (R = 0.38) and high RMSE (0.98 m) averaged across the study sites, with improved performance at 500 m resolution (R = 0.59, RMSE = 0.69). The distribution of Sentinel-1 and lidar snow depths is more similar in regions of deeper snow ($\triangle$ NRMSE = 0.078 mm^{-1}), lower forest coverage ($\triangle$ NRMSE = 0.019 m %$^{-1}$), higher incidence angles ($\triangle$ NRMSE = 0.002 mo^{-1}), dry snow, and at coarser spatial resolutions. This study marks the first open-source SAR technique for snow depth retrievals, thereby providing insight into the applicability of C-band SAR for snow depth retrievals and how to synthesize this technique with other snow property estimations.

1   Introduction

Runoff from seasonal snow provides water for billions of people (Barnett et al., 2005; Mankin et al., 2015), supplies ∼70 % of the annual discharge in the western United States (WUS; Li et al. (2017)), generates clean hydroelectric power, and supports multi-billion dollar agricultural and recreation industries with the total value of seasonal snow estimated in the trillions of

dollars (Sturm et al., 2017). Understanding the spatial distribution of seasonal snow water equivalent (SWE), the defining hydrologic variable of the snowpack, is essential for the effective management of this critical resource (Bales et al., 2006). Measuring SWE requires knowledge of snow depth and density, with snow depth spatial variability providing the majority of the variation in SWE values (Sturm et al., 2010). Therefore, accurately measuring snow depth over watershed scale regions is crucial for global SWE estimation.

Current snow depth measurement techniques lack either the spatial or temporal resolution necessary to accurately monitor basin-scale snow depth patterns for a variety of scientific and resource management applications (Sciences, 2018). Networks of in situ weather stations (e.g., SNOTEL in the United States) make point measurements of snow depth with high temporal resolution, but accurate interpolation required to generate distributed products presents a significant challenge (Dressler et al., 2006; Bales et al., 2006; Schneider and Molotch, 2016). High-resolution commercial stereo imagery (Shaw et al., 2020), airborne lidar (Currier et al., 2019; Deems et al., 2013) and structure-from-motion (Bühler et al., 2016; Nolan et al., 2015; Miller et al., 2022; Meyer et al., 2022) provide distributed snow depth maps for areas without canopy cover at meter to submeter-scale spatial resolutions with moderate accuracy (RMSE = 5-25 cm; McGrath et al., 2019; Currier et al., 2019; Deems et al., 2013). The Airborne Snow Observatory (ASO; Painter et al., 2016) and the Canadian Airborne Coastal Observatory produce operational snow depth maps using aerial lidar in mountain basins across the western North America. However, logistical constraints (e.g., cloud cover, tree canopies, platform range, expense) typically limit acquisition frequency and spatial coverage. Spaceborne lidar has shown promise for measuring snow depth, yet currently has high uncertainties (0.5–2 m) in complex terrain and only provides non-repeating linear transects of point-based returns (Enderlin et al., 2022; Deschamps-Berger et al., 2023). Measurements from spaceborne passive microwave instruments (Kelly and Chang, 2003; Takala et al., 2011) can be used to produce distributed snow depth products with 12-hour temporal resolutions. However, passive microwave measurements saturate in dry snowpacks approximately 0.8 m deep (Tedesco and Narvekar, 2010; Smith and Bookhagen, 2018), which represents a small fraction of total snow depth in some regions, and retrievals are unreliable over complex topography (Tong et al., 2010). Given the challenges and limitations associated with existing methods, other techniques are under development to produce spatially-distributed snow depth measurements.

Synthetic aperture radar (SAR) is a promising technique to complement existing snow depth monitoring. SAR is an active microwave-based system that can operate in all weather conditions, does not rely on solar illumination, and is capable of meter-scale resolution from spaceborne platforms. SAR signals interact with the snowpack, allowing for measurements of snowpack properties (Rosen et al., 2000; Tsai et al., 2019; Marshall et al., 2021). Thus, SAR methods for retrievals of snow depth and SWE have the potential to meet the National Academy of Sciences 2018 Decadal Survey requirement of snow depth and SWE measurements at ∼100 m spatial resolution (Sciences, 2018). However, SAR-based methods for retrieving snow depths are relatively immature and require additional investigation to understand limitations before they can be operationalized. This study provides an independent validation across multiple sites in the WUS of a recent SAR-based technique for retrieving snow depth (Lievens et al., 2022). We compare the SAR-based snow depth retrievals to highly accurate, lidar-derived snow depth measurements (Abedisi et al., 2022).

1.1 SAR volume scattering snow depth retrieval theory

SAR sensors emit electromagnetic energy in the microwave range (1–40 GHz) and measure the amplitude and phase of the backscattered (returning) wave. Depending on the radar wavelength, microwaves can be transmissible through snow, but when the wavelength is similar to the diameter of snow grains ($\sim$0.1–5 mm) or thickness of snow layers ($\sim$1–10 cm), volumetric scattering occurs as the microwaves interact with individual grains within the snowpack (Naderpour et al., 2022; Tsang et al., 2022). Hence, for SAR wavelengths at C-band or smaller, the presence of snow increases volumetric scattering relative to non-snow conditions. At non-zero local incidence angles, the volumetric scattering increase causes an increase in backscatter returning to the sensor, as less energy reflects off the ground and away from the sensor and more energy scatters back towards the sensor. Some SAR-based methods exploit the increased volumetric backscatter to retrieve snow properties including depth and SWE (Tsang et al., 2022).

A variety of different SAR frequencies have been explored for volume scattering retrievals of snow depth, with the ideal frequencies using millimeter-scale wavelengths close to the size of individual snow grains (Rott et al., 2010; Tsang et al., 2021). However, C-band volume scattering signals also hold promise for snow depth retrievals. Specifically, snow depth retrievals derived using C-band SAR from the European Space Agency's (ESA) Sentinel-1 (S1) satellite constellation (5.405 GHz, $\sim$5.55 cm wavelength) have been compared to in situ measurements and shown to accurately retrieve snow depths (mean absolute error = 0.18 m) at continental scales (Lievens et al., 2019).

The relationship between C-band volume scattering and snow depth is an ongoing area of investigation. Many previous studies have concluded that under dry snow conditions, the majority of the backscattered energy comes from the ground, depending primarily on soil temperature and moisture content. These results align with microwave scattering theory as the wavelength at C-band is too large to be scattered by individual snow grains, which are typically <5 mm. Two previous studies using tower-mounted radar (Strozzi et al., 1997; Mätzler, 1987) and aerial radar (Bernier and Fortin, 1998) showed either a slight decrease or no relationship between C-band backscatter and snow presence. These initial studies suggested that dry snow has almost no volumetric scattering at C-band and any mid-winter changes in backscatter would be either overwhelmed by the soil backscatter signature (Strozzi et al., 1997), or were caused by variations in the soil dielectric constant due to varying thermal insulation from the snowpack (Wegmüller, 1990; Bernier et al., 1999; Sun et al., 2015). However, these studies were limited by very shallow (<1 m depth) snowpacks (Bernier and Fortin, 1998; Fuller et al., 2009), co-polarized backscatter (Mätzler, 1987; Fuller et al., 2009; Shi and Dozier, 2000), or an inconsistent ground footprint (Strozzi et al., 1997).

Other studies have shown that dry snowpacks are not fully transparent at C-band especially in the horizontal orientation. A study using artificial snow showed a 5 dB cross-polarized (orthogonal transmitting and receiving antennas) backscatter increase with a 1 m snow depth increase (Kendra, 1995). Two recent tower-based studies showed a 2–5 dB increase in co-polarized (parallel transmitting and receiving antennas) backscatter for C-band (Naderpour et al., 2022) and significant volume scattering from C-band cross-polarized backscatter at snowpack layering interfaces (Brangers et al., 2023). More recently, the development of dense media radiative transfer (DMRT) models has suggested that anisotropic clusters of snow grains may produce more cross-polarized backscatter from within the snowpack volume at C-band than previous isotropic scattering models
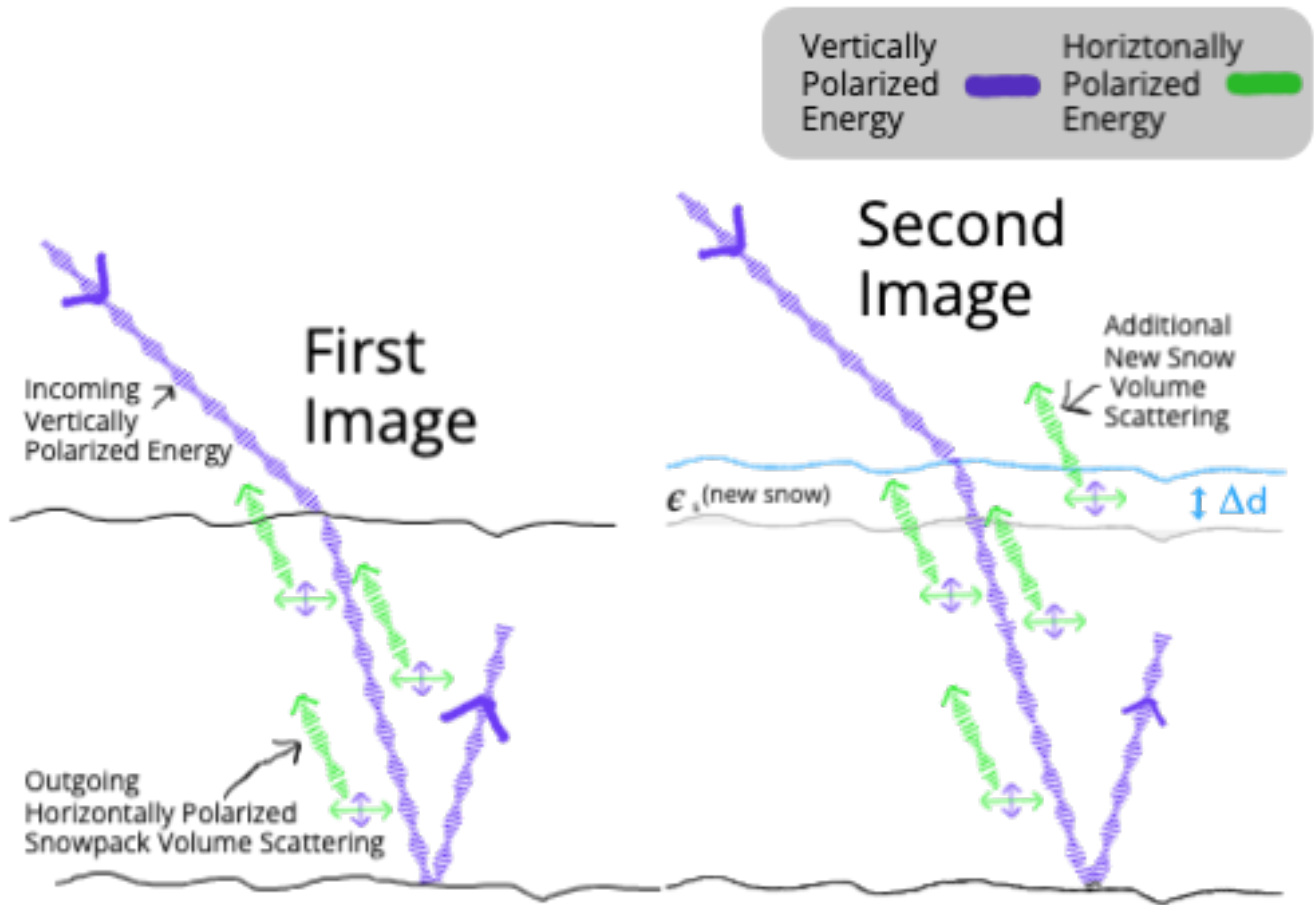
Figure 1. Conceptual figure showing the increases in cross-polarized backscatter with new snow accumulation.

suggested (West, 2000; Ding et al., 2010; Chang et al., 2014; Zhu et al., 2023). The increase in cross-polarized backscatter from these clusters may be sufficiently large to allow for measurements of snow depth changes as new snow increases the cross-polarized energy that is backscattered toward the sensor (Figure 1).

Following these theoretical results, Lievens et al. (2019) developed a time series based algorithm using the ratio of VH (cross-polarized) to VV (co-polarized) backscatter from S1 imagery to map snow depth at one-kilometer resolution. This algorithm includes three empirically derived "fitting parameters", which are tuned to minimize differences compared to land surface model output. Their initial results over the Northern Hemisphere showed mean absolute errors (MAE) of 0.31 m when compared to in situ station measurements. This cross-polarized ratio-based approach reduces the impacts of changes in the soil and geometric signals, which would impact both polarizations, and isolates the snow signal, which should primarily change the cross-polarized backscatter. The technique was further refined in a subsequent study by Lievens et al. (2022) over Switzerland and Austria, where they compared the spaceborne retrievals to modeled snow depth changes, with Pearson correlation (R)

> 0.7. The best results were achieved in regions with snow depths greater than 1 meter, forest cover fraction (FCF) less than 80 %, and elevations higher than 1000 m. This study also evaluated snow depth retrieval accuracy at spatial resolutions of 100 m, 500 m, and 1000 m and incorporated information from the change in VV backscatter for heavily forested regions. Their sub-kilometer retrievals also compared well to in situ stations ($R = 0.87$, MAE = 0.17 m; Lievens et al., 2022). Finally Lievens et al. (2022) also introduced a wet snow flagging mechanism based on using thresholds of backscatter change to flag pixels as wet or refrozen. These flags could then be used to identify lower confidence retrievals in the wet snow.

These S1-based snow depth retrieval studies show promise, but have only been validated against point-based in situ measurements and modelled snow depths at 1 km spatial resolution. Additionally, the impact of the snow depth detection algorithm's fitting parameters on accuracy retrieval has not been evaluated. Evaluating the relative value of these fitting parameters allows us to evaluate the information in the cross-polarized C-band signal compared to regional optimization of model parameters. The algorithm's wet snow flagging thresholds have also not been evaluated as to their relative impacts on performance and percentage of pixels marked wet.

1.2 Research objectives

Our primary goals for this study are to evaluate the relationship between S1 cross ratio (VH -VV) backscatter and lidar snow depths, the effectiveness of the snow depth retrieval technique introduced by Lievens et al. (2022) and to further clarify where and when this technique will be effective. To these ends, we target three main research objectives:

1. Identify if there is a relationship between S1 cross ratio backscatter changes and lidar snow depths.

2. Quantify the performance of Lievens et al. (2022)'s S1 snow depth retrievals using the SnowEx lidar datasets.

3. Quantify algorithm accuracy with respect to forest canopy cover, absolute snow depth, elevation, aspect, and spatial resolution.

These objectives are motivated by the U.S. National Academy of Sciences 2017–2027 Decadal Survey for Earth Science and Applications from Space (Sciences, 2018), which targets snow depth and SWE measurements in the mountains at 100 m spatial resolution. The current study works toward these targets by assessing how and where globally available snow depth retrievals from S1 could be incorporated into any future synthesis snow depth products.

2 Methods

We organize our methodology into five subsections. First, we describe the datasets used in the S1 algorithm and for validation. We then describe the S1 snow depth retrieval algorithm, parameter optimization and performance evaluation.
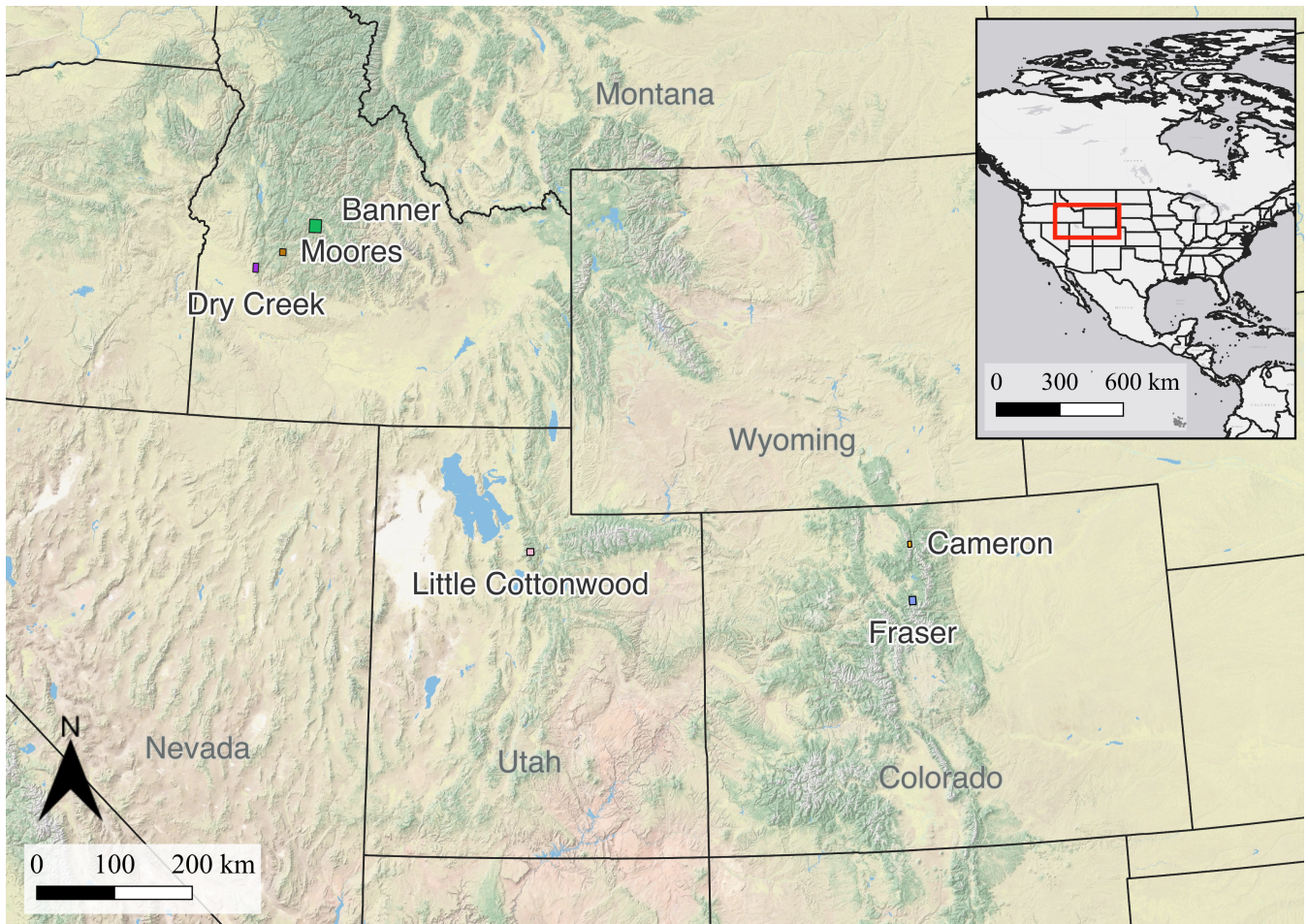
Figure 2. Bounding boxes of airborne lidar collected at the NASA SnowEx sites.

2.1 Datasets

2.1.1 Sentinel-1 images

The S1 mission is a constellation of one to two (at various points in its history) polar-orbiting satellites that acquire C-band (5.405 GHz or 5.55 cm) SAR data with a 12-day orbital cycle. We used S1 images acquired in interferometric wide (IW) swath mode (250-km swath width) which has a spatial resolution of 22 m in azimuth (i.e., along-track direction) and 2.7–3.5 m in range (i.e., across-track direction) depending on the incidence angle. Measurements made over land surfaces in IW mode are dual-polarized — vertical–vertical (VV) and vertical–horizontal (VH). The overlapping swaths captured by S1 from different orbits result in 2–3 day revisit intervals for mid-latitudes and up to daily revisits at polar latitudes.

S1 images were processed using the Alaska Satellite Facility's HyP3 (Hogenson et al., 2020) pipeline to produce radiometrically terrain corrected (RTC) gamma-naught backscatter images using GAMMA software (Frerebeau et al., 2023; Lebrun et al., 2020) and the GLO-30 Copernicus DEM (European Space Agency, 2021). The processing included precise orbit file application, border noise removal, thermal noise removal, radiometric calibration, range-doppler terrain correction, and terrain flattening to produce gamma-naught images at 30-m resolution. All images were averaged in linear scale to 90-m resolution. For each study site (Section 2.1.2), all S1 images that overlapped the lidar flight's bounding boxes were downloaded starting 1 August of the corresponding water year until two weeks after the lidar acquisition date, resulting in 607 S1 images (Table 1).

2.1.2 SnowEx lidar acquisitions

Table 1. Overview of study sites

Site Name	Center Coordinates	Area (km²)	Elevation Range (m)	Snow Classification (Sturm et al., 1995)	Vegetation Types	Lidar Flight Date(s)	S1 Images	Notes
Cameron	-105.88980, 40.53842	22.1	2,897 - 3,711	Boreal Forest (92%) Montane Forest (4%) Tundra (4%)	Alpine Tundra Subalpine Forests Subalpine Meadows	2021-03-19	59	
Fraser	-105.89437, 39.88454	63.2	2,667 - 3,800	Boreal Forest (57%) Montane Forest (40%) Tundra (3%)	Alpine Tundra Subalpine Forests Subalpine Meadows	2020-02-11 2021-03-19	50 59	2020 Li-DAR flight covers smaller area (36.2km²)
Little Cottonwood	-111.66790, 40.55951	28.1	1,983 - 3,457	Tundra (35%) Boreal Forest (30%) Montane Forest (31%) Prairie (4%)	Subalpine Forests Subalpine Meadows	2021-03-18	80	
Banner	-115.18431, 44.26822	168.7	1,566 - 2,820	Montane Forest (40%) Boreal Forest (20%) Prairie (20%) Tundra (20%)	Alpine Tundra Subalpine Forests Subalpine Meadows	2020-02-18 2021-03-15	58 97	Banner SNOTEL Info: ID: 312, Elevation: 2145m Loc: (44.33, -115.23)
Mores	-115.68530, 43.94584	34.7	1,551 - 2,469	Montane Forest (45%) Prairie (25%) Boreal Forest (18%) Tundra (12%)	Mixed Conifer Forests Subalpine Forests Sagebrush Steppe Subalpine Meadows	2020-02-09 03-15-2021	44 47	
Dry Creek	-116.10371, 43.74664	38.3	1,233 - 2,279	Montane Forest (97%) Prairie (3%)	Sagebrush Steppe Ponderosa Pine Forests Grasslands	2020-02-19	83	

2.1.3 Ancillary datasets

The S1 snow depth retrieval algorithm requires forest cover fraction (FCF) and snow presence ancillary datasets in addition to S1 imagery. Following the procedure outlined in Lievens et al. (2022), we used the Copernicus Global Land Service Proba-V land cover dataset (Buchhorn et al., 2020) at 100 m resolution to quantify FCF and mask open water areas. We delineated snow presence using the Interactive Multisensor Snow and Ice Mapping System (IMS) (NSIDC, 2008), a daily binary snow cover product at 1 km spatial resolution. For visualizations, we incorporated snow depth data from a telemetered snow monitoring SNOTEL station (Banner ID:312) (Schaefer and Paetzold, 2000).

2.2 Snow depth retrieval algorithm

We implemented a fully reproducible, open-source Python version (Hoppinen et al., 2023) of the S1 algorithm introduced by Lievens et al. (2022). The central equation of this pixelwise, ratio-based approach can be written as

$$\Delta SD = C \left[(1 - FCF) \cdot \Delta(A\gamma_{\mathrm{VH}}^0 - \gamma_{\mathrm{VV}}^0) + B \cdot FCF \cdot \Delta\gamma_{\mathrm{VV}}^0 \right] \tag{1}$$

and retrieves the snow depth (SD) within each S1 pixel using the forest cover fraction (FCF) and the S1 cross-polarized (γ_{VH}^0) and co-polarized (γ_{VV}^0) backscatter in units of of dB, as well as three empirical tuning parameters (A, B, and C). We note that subtraction of cross- and co-polarized backscatter in the logarithmic dB scale equates to a ratio in the linear power scale. The Δ operator in (Equation 1) denotes changes in various quantities including S1 backscatter values, which should be calculated using two images with the same orbital geometry (which may not be the two closest images in time).

We implement (Equation 1) only for pixels with snow present in the IMS data. Starting with zero snow depth on August 1 of a given year, we integrate the changes in snow depth through time. The three empirical parameters A, B, and C can be tuned in order to optimize performance. A is used to control the relative weight of the VH backscatter to VV in the cross-polarized ratio, while B controls the relative impact of co-polarized backscatter changes on the final snow depth retrievals. C is a slope parameter that controls the change in snow depth associated with the weighted combination of co- and cross-polarized backscatter changes.

Although our algorithm implementation generally follows the methods detailed in Lievens et al. (2019, 2022), notable deviations include:

- We used S1 RTC images processed with the GLO-30 Copernicus DEM instead of the Shuttle Radar Topography Mission (SRTM) DEM to avoid SRTM inaccuracies associated with snow cover in mountainous regions in North America during data collection in February 2000 (Tarricone et al., 2022).

- We implemented a 3×3 multi-looking during S1 image pre-processing, resulting in a spatial resolution of 90 m instead of 100 m.

- We used February 1 as the earliest date a pixel can be flagged as permanently wet snow to avoid erroneously flagging pixels for the remaining time series due to early season melt events.

Despite following the methods described in Lievens et al. (2022), our open source snow depth retrievals had a correlation to the retrieved snow depths from Lievens et al. (2022) of only 0.64 averaged across all sites. Apparently, the outlined methods in Lievens et al. (2022) are missing a few utilized techniques (H. Lievens, Personal Communication, December 25, 2023). These include: averaging backscatter changes relative to 6, 12, 18, and 24 days ago, using the wet snow flags to reduce wet snow influenced snow depth changes, and different averaging weight vectors for calculating the previous snow index. However, since the average correlation to the lidar across the nine sites was 0.003 better for our retrievals relative to the provided data we continued with using our higher spatial resolution, open-source retrievals following the described methods.

See Appendix A for a complete description of the S1 snow depth retrieval algorithm.

2.3 Parameter optimization and performance evaluation

Lievens et al. (2022) used parameter values $A = 2.0, B = 0.5, C = 0.44$ in (Equation 1) optimized using modeled snow depth data over Switzerland. Here we derive a new set of parameters optimized for the western United States. We find the optimal A, B, and C using the S1 image closest in time to the lidar acquisition. The time between S1 and lidar snow depth acquisitions was less than two days except for Mores 2020 (two days, one hour) and Fraser 2020 (five days, 13 hours) (Table 1). As in Lievens et al. (2022), we optimize the A and B parameters by maximizing R and the C parameter by minimizing mean absolute error (MAE) (Webster and Oliver, 2007) between the lidar and retrieved snow depths. We vary A between 1 and 3 by increments of 0.1, B between 0 and 1 by increments of 0.1, and C between 0 and 1 by increments of 0.01. We perform this optimization across all nine validation datasets to get a single WUS-optimized parameter set ($A = 1.5$, $B = 0.1$, and $C = 0.59$). A more thorough discussion of parameter optimization process and relative impacts on performance of each parameter is included in Appendix D.

We begin by comparing lidar snow depths against the S1 CR signal by summing the CR changes during periods of snow coverage (using the IMS snow cover data) and comparing the resulting snow season changes in CR to the lidar snow depths and to season-long snow depths from a SNOTEL station at Banner Summit.

After optimizing the algorithm parameters, we implement the S1 snow depth retrieval algorithm over each of the study sites for the duration of the snow season. We assess algorithm performance at each site by calculating RMSE and R between the lidar validation dataset and the S1 image closest in time to the lidar acquisition. We also examine performance with respect to various environmental and sensor-related factors, including absolute snow depth, forest cover fraction, aspect, elevation quantile within each site, and the spatial resolution of the S1 imagery used to derive snow depth.

3 Results

3.1 S1 cross ratio compared to snow depth

We began by evaluating the relationship between the S1 CR backscatter changes during the snow season and the lidar snow depths. At the Banner Summit 2021 Site we qualitatively observed significant (10-20 dB) of changes throughout the season in

the CR for the regions of higher snow depth along at high elevations. (Figure 3a, b). At lower-elevation regions with less snow we observe some significant decreases in CR throughout the season, likely due to wet snow effects. The time series of CR at the Banner site also showed increasing CR throughout the accumulation season (Figure 3c). For the pixels with less than 1 m of snow there was also a sigificant drop around March 1st that coincides with a loss of snow height at the SNOTEL station likely due to wetting effects. These relationships continued in the grouped evaluations of all nine study site's pixels (Figure 3d, e) with little change in pixels without snow (no wet snow or snow accumulation signals), significantly negative effects for the wet snow pixels with between 0.5-1 m of snow and finally significantly positive changes in CR for pixels with above 1.5m of snow depth. Finally an assessment of vegetation's impact on the CR showed limited relationship and a slightly negative relationship between the CR changes and the forest cover fraction of the pixels (Figure 3 f).

3.2 Algorithm performance evaluation

The S1 volume scattering retrievals at 90 m resolution showed moderate agreement when compared to all available lidar snow depths across all study sites (R=0.46), with ranges from R=0.02-0.54 for individual study sites (Table 3). RMSE for all pixels combined (n = 57,608) was 0.92 m with ranges from 0.65–1.07 m for individual sites. The performance improved at coarser spatial resolutions with the site-wide RMSE values improving by 0.18 m to 0.74 m at ~500m resolution and R increasing to 0.56 (Table 3). There was some additional improvement after coarsening to 1 km resolution (R = 0.64, RMSE 0.65 m) but this improvement was less substantial than the improvement from 90 m to 500 m spatial resolution.

Evaluation of improvements using just dry snow pixels relative the all pixels showed mixed results (Table 3). Three sites showed significant increases in correlation, one saw a significant decrease, and the remaining saw no significant changes in correlation. Notably Fraser 2020 even had a 0.24 decrease in correlation when using just the dry snow pixels The RMSE results were similar with most sites maintaining similar RMSEs between dry and wet flagged snow pixels.
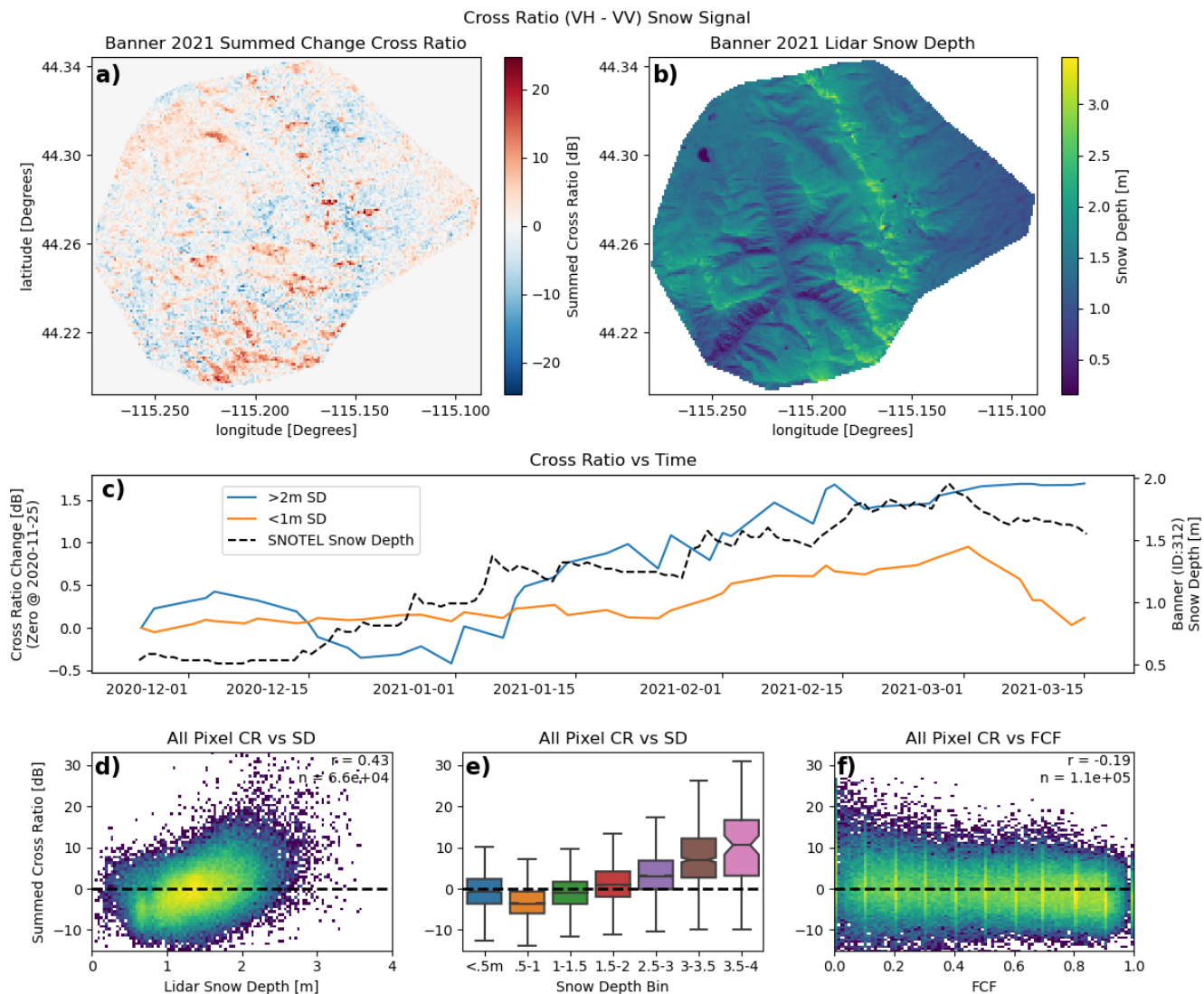
Figure 3. Visualization of changes in S1 cross ratio (VH - VV; CR) for periods with snow present in IMS data for Banner in 2021 (a), visualization of lidar snow depth for Banner 2021 flight (b), time series of changes in cross ratio (CR) relative to November 25th for pixels with under a meter of snow depth (orange) and pixels with over 2 meters of snow depth (blue) at the Banner site along with the Banner Summit SNOTEL snow-depth, (c), 2D log scaled histogram of summed cross ratio changes relative to lidar snow depth (d), box plots of summed CR for snow depth bins (notches show bootstrapped 95% distributions of the mean) (e), 2D log scaled histograms of summed cross ratio changes relative to forest cover fraction (FCF) (f).

Table 2. Evaluation of RMSE and Pearson R for all pixels (All) and exclusively dry-flagged pixels (Dry) for VV and VH. * represent correlation values with significant differences (Fischer z < 0.01) from the all pixel data.

Site	RMSE		R	
	All	Dry	All	Dry
All Sites	0.92	1.03	0.46	0.45
Banner 2020	1.00	0.92	0.40	0.37
Banner 2021	0.89	1.14	0.42	0.49*
Dry Creek 2020	0.74	0.78	0.21	0.24
Fraser 2020	0.93	1.26	0.38	0.14*
Fraser 2021	0.65	0.79	0.18	0.44*
Little Cottonwood 2021	1.07	1.17	0.54	0.51
Mores 2020	1.07	0.97	0.08	0.19*
Mores 2021	0.91	0.91	0.40	0.34
Cameron 2021	1.07	1.03	0.02	0.46
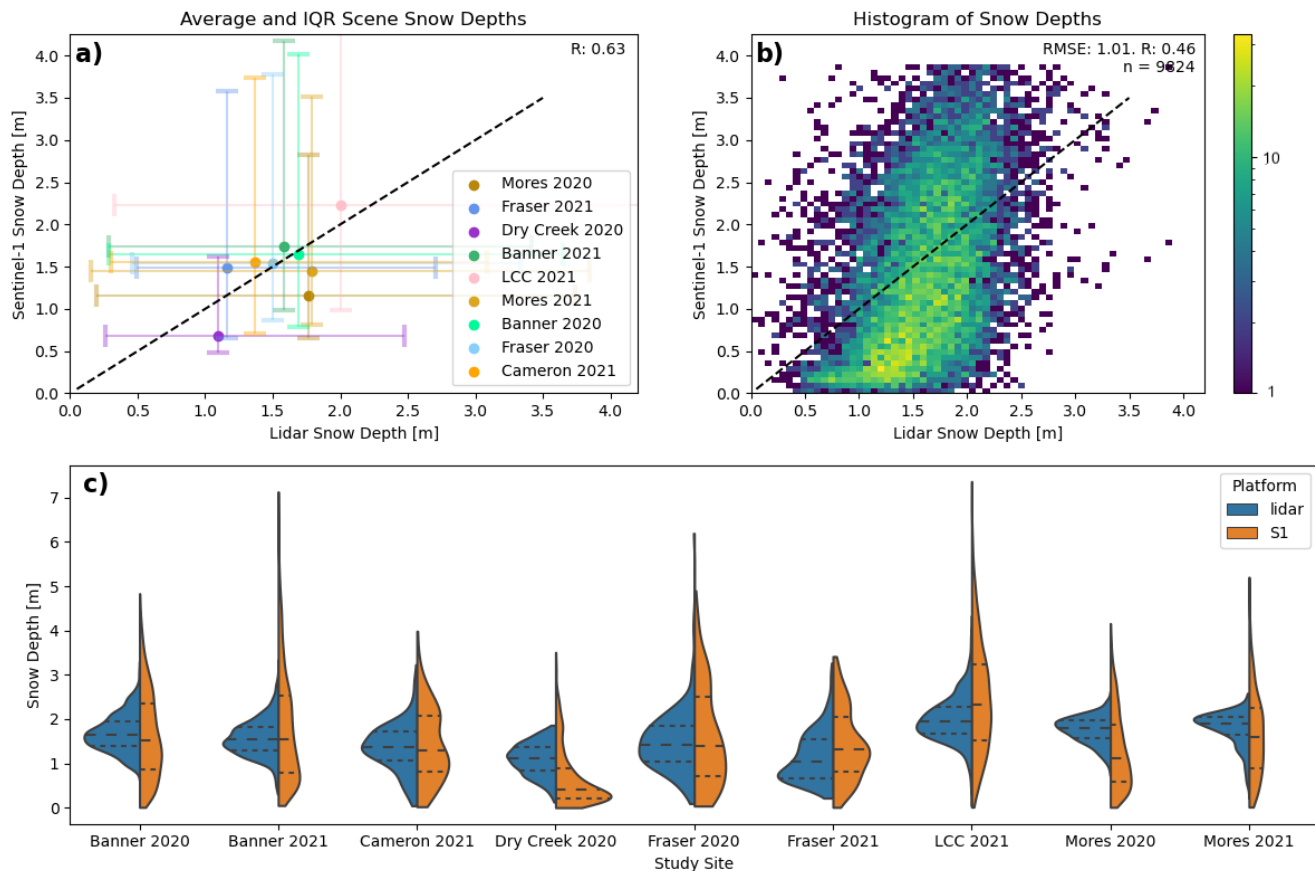
Figure 4. a) Mean lidar snow depths vs. mean S1 snow depths at each site, with error bars representing the 25th and 75th quantiles at each site, b) pixel-wise log-scaled 2d histogram of lidar vs. S1 snow depths, and c) site-by-site distributions of lidar and S1 snow depths. Note that only pixels flagged as dry snow and pixels with snow present in the IMS data were used in this analysis.

The site averages were close to the 1:1 line and generally followed the trends in lidar scene averaged snow depth (R = 0.63, Figure 4a). The pixel-wise comparison also showed worse agreement (R = 0.46, RMSE = 1.01 m). There seems to be a discontinuity around 1 m of snow depth with generally minimal changes in the retrieved snow depth below this ≈ 1 m of lidar snow depth and a sharp increase in the retrieved depths above it (Figure 4b). Finally, the distributions (Figure 4c) show

225   a variable result with Dry Creek 2020 showing a strong under-capture of snow depth and most other cites showing reasonable agreement and some long tails capturing outliers of 4+ meters of snow in the retrieved snow depths.

We use the Banner 2021 site to qualitatively illustrate the differences between the lidar and S1 snow depths (Figure 5). Lidar (Figure 5a) and S1 (Figure 5b) snow depths display similar spatial patterns (e.g., increasing snow depth with elevation) but the S1 algorithm estimates shallower snow depth across considerable portions of the study area (brown shades in Figure 5c). This

negative bias appears especially prevalent in regions at lower elevations (Figure 5d) and with high FCF (Figure 5e). Conversely, the algorithm overestimates snow depths in high elevation regions with less tree coverage.

To further examine algorithm performance, we explore the Banner 2021 results within the context of differences in absolute snow depth (measured by lidar), forest cover, elevation, snow type (dry vs. wet), terrain aspect, and spatial resolution of the S1 retrievals (Figure 6). Figure 6a indicates the underestimation bias of the S1 snow depth retrieval algorithm. S1 and lidar snow depths agree best in regions of low forest cover ($< 50\%$), and S1 underestimates snow in highly forested regions (Figure 6b). The elevation-dependent results in (Figure 6c) reinforce the general pattern visible in Figure 5e, with closer agreement at higher elevations and S1 underestimation at lower elevations. We note that this may partly due to the covariance between elevation and forest cover at this study site. Similar to Lievens et al. (2022), we found that the S1 retrieval underestimates snow depth in wet snow (Figure 6d). The algorithm also shows decreased performance over north and west aspects than it does over south and east aspects (Figure 6e). Finally, we find increased agreement between lidar and S1 snow depths at coarser spatial resolutions.

Evaluation of the binned snow depth, forest cover fraction, elevation, aspect, and spatial resolution across all nine validation datasets (Figure 7 a-d) shows similar results to those from Banner 2021. We saw decreasing mean-normalized RMSE with higher snow depths, less forest coverage, higher elevations, and coarser resolution (Figure 7). The average change in NRMSE per meter increase in snow depth was $-1.06\,\mathrm{m\,m^{-1}}$ ($p < 10^{-4}$), forest cover fraction percentage was $0.038\,\mathrm{m\,\%^{-1}}$ ($p < 10^{-6}$), elevation was $-2.61\mathrm{mm^{-1}}$ ($p < 10^{-4}$). The aspect relationships were more complex and showed a minimum in nRMSE for south, east, and due north aspect with increasing nRMSEs for west and north-east (Figure 7d). We also found an improvement in NRMSE at coarser spatial resolutions with non-linear decreases in NRMSE for all the sites. This non-linear shape suggests decreasing performance improvements at coarser spatial resolutions (Figure 7e). In summary, the S1 snow depth retrievals performed best in dry deep snow at mid-high elevations with forest cover below 50 % at spatial resolutions of 300 m or coarser.

4   Discussion

4.1   Cross Ratio Signal

Our evaluation of the changes in S1 CR backscatter match previous work (Lievens et al., 2019, 2022; Lund et al., 2022; Zhu et al., 2023) with significant increases in the CR signal observed for regions with deep snowpacks (>1.5 m), significant decreases observed for shallow snowpacks that are likely affected by wet snow (<1.5 m), and no significant changes observed in regions without snow in the lidar acquisitions (Figure 3). Additionally we evaluated the potential covariance of the CR changes with vegetation and found a weak and negative correlation (R = -0.19). These suggest that there is a relationship between the C-band S1 backscatter and snow depths but that other factors, especially snow wetness, are significant challenges.
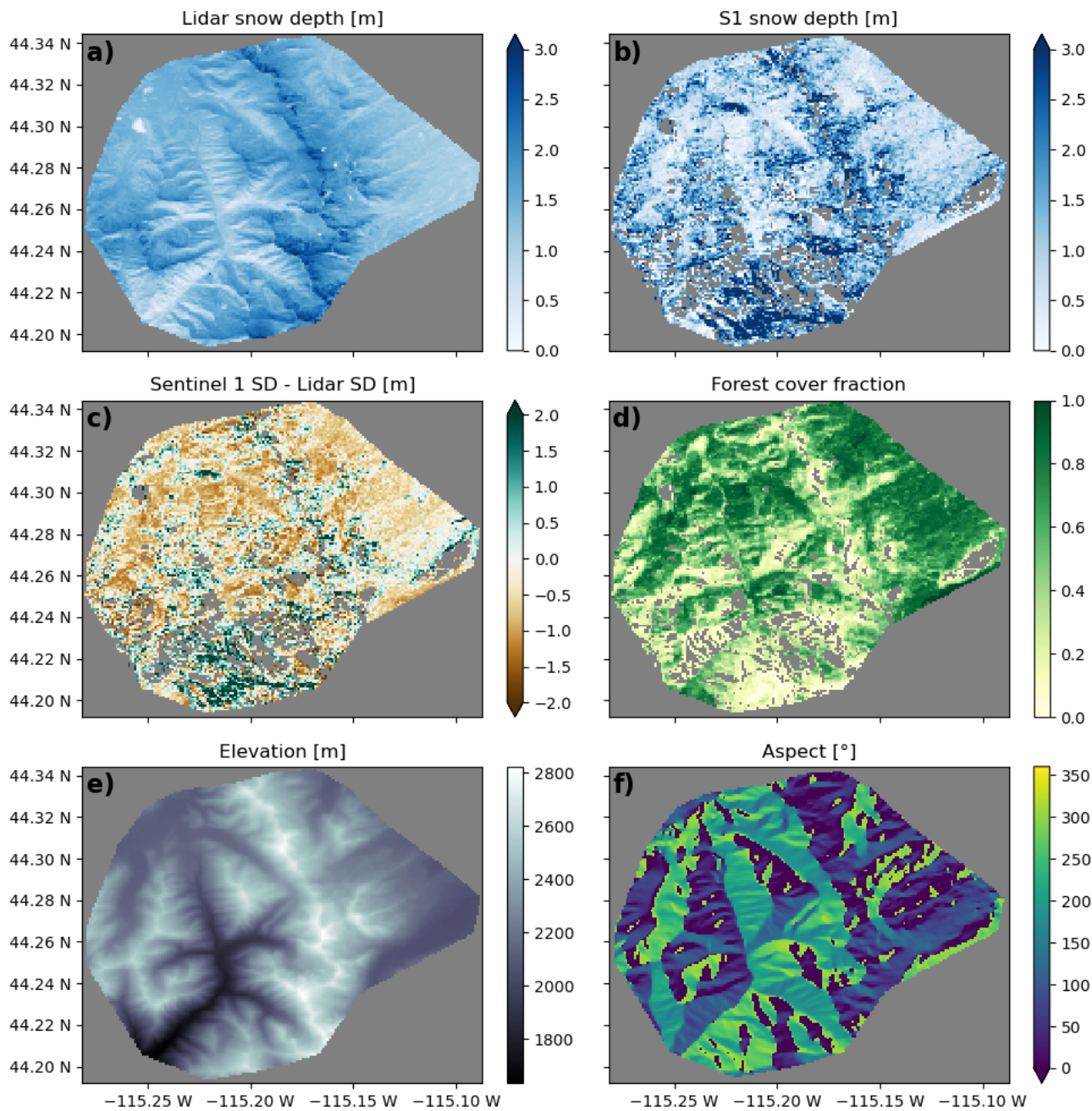
Figure 5. Banner 2021 visualizations of lidar snow depth (a), retrieved snow depth (b), difference between lidar and retrieved snow depth (c), forest cover fraction (d), elevation (e), and aspect (f).
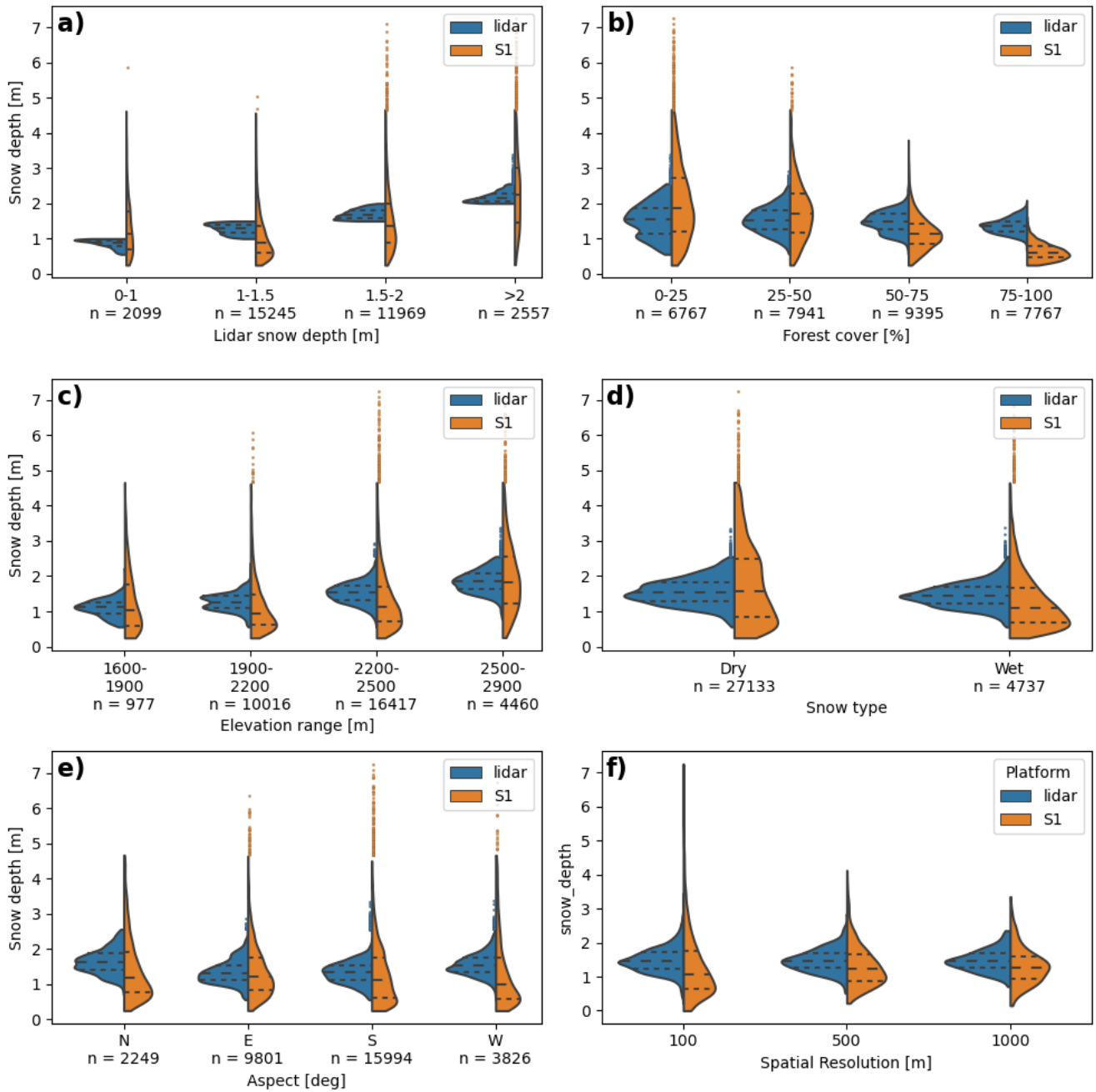
Figure 6. Distributions of lidar and retrieved snow depths at Banner 2021 subset by snow depth (a), forest cover (b), elevation (c), wet snow flagging (d), aspect (e), and spatial resolutions (f). Values between the 1st–99th percentiles are incorporated into the distributions, while outliers beyond this range are indicated with blue or orange points.
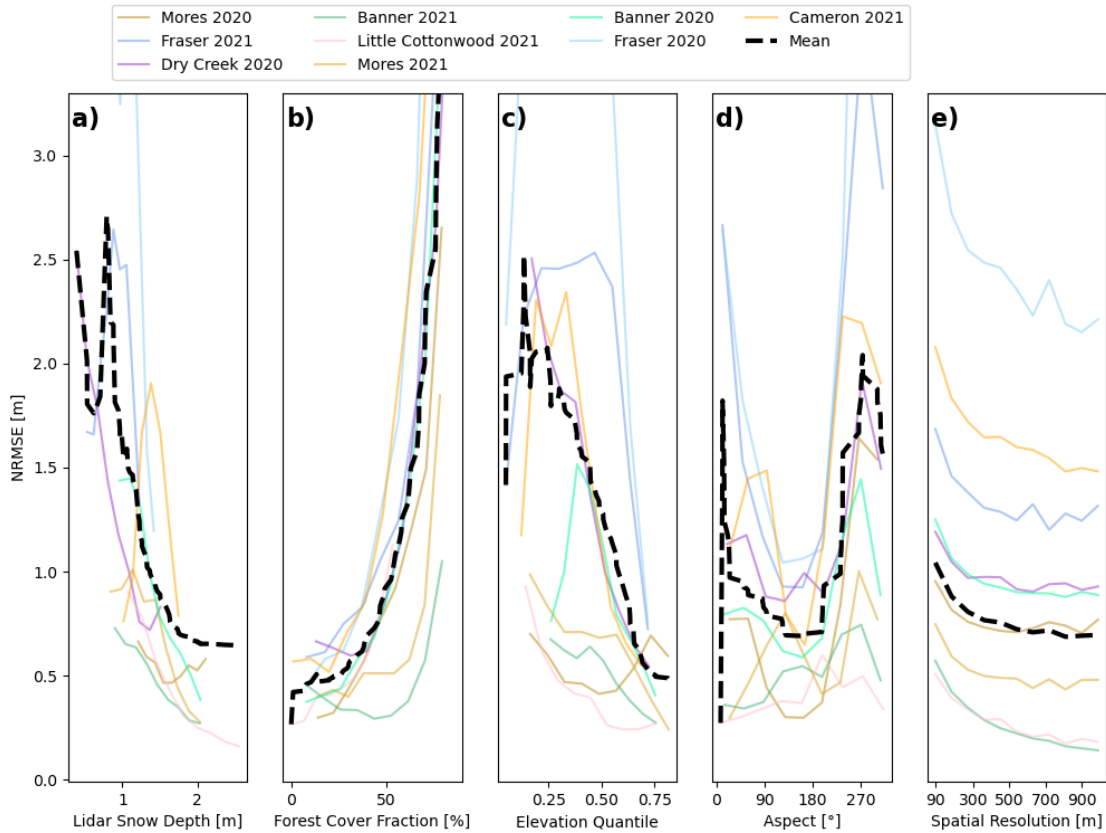
Figure 7. Site-by-site mean-normalized RMSEs along with grouped means (excluding low correlation sites - Fraser 2020, Mores 2020, Cameron 2021) for bins of lidar snow depth (a), forest cover fraction (b), elevation quantile (c), aspect (d) and spatial resolution (e). Elevation was normalized between 0 and 1 at each site to improve comparison of the intra-site trends.

4.2 Snow depth retrieval accuracy

260 Our results show that S1 backscatter algorithm proposed by Lievens et al. (2022) can minimally reproduce the spatial distribution of snow depth when compared to airborne lidar, but correlations values were low, with an average of 0.36 across all nine sites. This technique also struggles in specific years and locations, with three sites achieving correlations below 0.2 and and RMSEs > 1 m at four sites. Favorable sites show correlations of close to 0.5 (Table 3). RMSEs of around 0.6–0.7 m for an entire season were observed at three sites, dropping close to 0.5 m at coarser spatial resolutions. These RMSEs improve at

265 coarser spatial resolutions (Figure 7e), but even then no site had RMSEs below 0.5 m. Our results suggest that S1 backscatter can add information to existing snow monitoring systems by providing high temporal density and spatial coverage, but that

alternative retrieval algorithms should be explored and the technique should be used with a full understanding of its limitations and high uncertainties.

The dry flagged pixels had variable performance relative to using the entire dataset. This could be either due to similar performance between wet and dry snow, but this is unlikely based on previous findings and the lower signal-to-noise ratio in wet snow (Ruiz et al., 2022). A more likely answer is that the wet-snow flagging was incorrectly identifying wet snow pixels and could use a more sophisticated future algorithm. OR vast majority are wet or dry already.

To improve our understanding of when and where water monitoring technique should apply and use this technique we evaluated how the algorithm's performance varied with geophsyical parameters. We noted statistically significant relationships between the algorithm's NRMSE and snow depth, elevation and forest coverage (Figure 7a, b, c). These suggest that using this technique in deep dry snow conditions, with FCF below 50% and at high elevations will improve the algorithm accuracy. FCF seems to have the largest impact on RMSE, followed by total snow depth and then elevation. The relationship to FCF is expected due to the large amounts of volume scattering in vegetation potentially overwhelming the subtle changes due to snow volume changes (Vreugdenhil et al., 2020). Lower RMSE at higher elevations is also expected due to lesser influence from wet snow. Finally, improvements in performance with deeper snow depths also make sense conceptually due to increased volume scattering at these deep depth. The histogram in (Figure 4b) shows this pattern of higher correlation at deeper snow depths and also to show a discontinuity in this relationship. There is almost no change in retrieved snow depths until ~ 1 m after which there is a strong increase in retrieved snow depths. This suggests there may a discontinuous regime change at around 1 m. All of these finding generally agree with those seen in Lievens et al. (2022).

The relationship between aspect and algorithm performance (Figure 7d) is likely some unknown combination of incidence angle and wet snow affects. South and north facing slopes, which have less extreme variation in incidence angle for polar orbiting satellites, might be expected to be less affected by radar shadow and layover. While we did see lower RMSEs on south faces, supporting this theory, we also saw increasing NRMSE for North faces. Additionally aspect controls both deposition, with east faces getting more wind-loading in the WUS, and melting, with south aspects getting warmer and wetter in the Northern hemisphere. These might lead you to expect higher errors on south faces, which we again didn't see, or lower normalized errors on eastern aspects, which we also didn't see. Overall the impact of aspect on algorithm performance is still unclear and future work should investigate it further.

Finally, at 90 m spatial resolution, this technique has quite high RMSEs that limit it utility as a method of accurately capturing snow depth at individual pixels. However, coarser averages of S1 snow depth and lidar snow depth typically agree better, suggesting that this technique can provide information about larger-scale snow patterns that may be valuable for water managers and hydrologic modeling. These improvements seem to be quite steep up to around 300-500 m spatial resolution (Figure 7e). At coarser resolutions there was not appreciable improvements in NRMSE. This improvement when averaging over larger areas is likely related to the subtle signal of the snow volume scattering at C-band relative to background noise from orbital errors, SAR speckle, variations in ground and vegetation properties, and other sources.

4.3 Limitation

We found reasonable evidence that the S1 CR backscatter contains a significant snow depth signal across the snow accumulation period (section 3.1) but also that the algorithm proposed in Lievens et al. (2022) struggles to convert those backscatter changes into reliable snow depths that recreate snow depths in diverse regions and across years (section 3.2). In implementing this algorithm it was challenging to evaluate what effects the parameter optimizations, time series smoothing, and ancillary datasets were adding to the existing snow information captured in the C-band CR signals. We suggest that future algorithms should consider a physically based model that would improve the transparency of the retrievals. A physically based model would also allow for an easier exploration of the impacts of potentially covariated signals including soil temperature, soil moisture, vegetation, and snow wetness. Alternatively, a machine-learning based approach that would take advantage of a much higher number of parameters to improve performance in converting the snow depth signal into reliable and consistent snow depths. Regardless anyone implementing the current algorithm should be aware of the large uncertainties in the retrieved snow depths.

4.4 Future work

Future work should evaluate the performance of this algorithm in prairie and Arctic snow regimes and further explore the impact of geophysical parameters such as ground roughness, liquid water content, vegetation type and height, and thermal properties of the ground. Given the aforementioned weaknesses of this algorithm (high RMSEs and middling spatial correlations) and optimization scheme (need for apriori data to set parameters), future studies could propose new approaches for retrieving snow depth from volume scattering signals at C-band, including other empirical or machine learning approaches. Future work should also investigate how these retrievals could effectively integrate into future remote sensing systems and modeling workflows to improve operational measurement and forecasting of snow depths.

This study used the same ancillary datasets for snow covered area and FCF as Lievens et al. (2022) to ensure a comparable analysis of these methods at the catchment scale. Snow depth retrieval accuracy may be improved by substituting alternative snow cover, FCF, and snow melt products. The binary nature and one-kilometer spatial resolution of the IMS snow cover product, for example, is likely inadequate for 90 m spatial resolution snow depth retrievals. Future work should consider other advanced snow cover data including spectrally-derived products from optical satellite imagery (Bair et al., 2021; Rittger et al., 2020), which show high correlation to finer resolution lidar-based snow cover retrievals (Stillinger et al., 2022). While the 100 m Copernicus Proba-V FCF product has been shown to work well for identifying forest cover and water bodies (Fuster et al., 2020), future work should look to higher resolution FCF data, for example from the National Land Cover Database which provides FCF and other land cover information at 30 m resolution (Homer et al., 2020).

To identify periods where S1 snow depth retrievals are likely to have poor accuracy, a snowmelt onset product such as Gagliano et al. (2023) could be integrated into snow monitoring operations. This could also be utilized by water managers to identify when the onset of stream flow is to be expected each season.

Finally, a metric of confidence and/or uncertainty for this dataset would be valuable for future synthesis with other remotely sensed and modeled datasets. While out of scope of this study, a potential metric should attempt to capture three factors: 1)

variability in VV throughout the winter season, 2) variability in VH throughout the winter season, 3) whether a pixel contains wet snow during imaging. A pixel with a large and reliable snow signal would have some significant variability in VH, relatively little variability or noise in VV, and would have dry snow. Since the algorithm already contains a flagging mechanism for dry vs. wet snow we can capture the third element already. Future metrics would also ideally be agnostic to ancillary datasets to the greatest degree possible to allow for calculation of this metric globally and at any resolution.

5 Conclusions

Our results present the first independent evaluation of a promising S1 volume scattering-based snow depth retrieval algorithm proposed by Lievens et al. (2022). We show strong and significant relationship between lidar snow depths and the S1 CR for regions with over 1.5 m of lidar-measured snow depths. For regions below 1.5 m we see decreases in the CR likely due to wet snow impacts. S1 snow depth retrievals from the CR improved as spatial resolution was made coarser (RMSE = 0.98 m, R = 0.33 at 90 m resolution; RMSE = 0.69, R = 0.59 at 500 m resolution). We also found performance improvements below 50 % forest cover fraction, dry snow conditions, south faces, and higher elevations. These results show the potential of these C-band volume scattering retrievals and provide an analysis of when, where, and how they could be effectively integrate with other snow estimation techniques.

Code availability. The repository for running Sentinel-1 snow depth retrievals using this algorithm is available at: github.com/SnowEx/spicy-snow. Analysis and figure creation code is available at: github.com/ZachHoppinen/spicy-analysis

Appendix A: Sentinel-1 Snow Depth Retrieval Algorithm Details

A1 Preprocessing Sentinel-1 imagery

We downloaded Sentinel-1 (S1) imagery using the Alaska Satellite Facility HyP3 (Hogenson et al., 2020) pipeline. To achieve a similar spatial resolution used by Lievens et al. (2022), we coarsened the S1 images from their native 30 m spatial resolution to 90 m resolution by averaging within a 3×3 pixel window using backscatter data in the linear scale. We then converted the backscatter data to logarithmic scale (units of dB) at the new 90 m resolution for use in all subsequent processing steps. All remaining pre-processing steps were performed on four subsets of the data based on the direction of satellite travel (ascending vs. descending) and acquiring satellite (S1A vs. S1B).

Most of our mid-latitude study areas exist within multiple S1 frames, and the relative location of the site in the frame can change based on the satellite orbit geometry. Different S1 orbit geometries (also called relative orbits) produce images with more or less backscattered power as a function of high vs. low local incidence angles. To account for changes in backscatter caused by differences in incidence angle (rather than changing conditions at the surface) we normalized the images from each

S1 orbit geometry. For each specific orbit geometry and polarization, we applied a constant shift to all images so that the mean of a particular image matched the overall mean for the given orbit geometry and polarization.

To correct for outliers, we calculated the 10th and 90th percentiles of backscattered power for each polarization and subset of images. We then masked any values that were 3 dB above the 90th percentile or 3 dB below the 10th percentile. We also masked out pixels with local incidence angles greater than 70 degrees to avoid regions of radar shadow. Finally, we recombined the four subsets of S1 images back into a single time series for each study site.

A2 Snow depth retrievals

The retrieval algorithm relies on the assumption that no snow exists on the surface at the beginning of the timeseries (we use August 1st for the Northern Hemisphere). Snow depth is calculated iteratively by attributing increases in backscatter to increases in snow depth. The IMS snow presence dataset) (NSIDC, 2008) is incorporated to avoid misattributing backscatter changes from other non-snow factors. Snow depth at each pixel is set to zero until the IMS dataset indicates snow presence, and snow depth is also set to zero after melt-out.

The primary S1 input to the snow depth retrieval algorithm is the cross-ratio of co- and cross-polarized backscatter. The cross-ratio is calculated at every valid pixel (i) over all available image acquisitions (t) by taking the ratio of VH to VV backscatter in a linear scale, or equivalently by subtracting VH from VV in a logarithmic [dB] scale:

$$\gamma^0_{CR}(i,t) = A\gamma^0_{\mathrm{VH}}(i,t) - \gamma^0_{\mathrm{VV}}(i,t) \tag{A1}$$

where A is an empirical fitting parameter used to control the relative weight of the VH backscatter to VV.

Next, two backscatter change variables are calculated between the image at the current timestep (t) and the prior timestep (t_{pri}). Depending on the study site and orbit geometries, the time elapsed between t and t_{pri} can be 6, 12, 18, or 24 days. The change in the cross-polarized to co-polarized backscatter ratio ($\Delta\gamma^0_{\mathrm{CR}}$) is given by

$$\Delta\gamma^0_{\mathrm{CR}}(i,t) = \gamma^0_{\mathrm{CR}}(i,t) - \gamma^0_{\mathrm{CR}}(i,t_{\mathrm{pri}}) \tag{A2}$$

and the change in the co-polarized backscatter ($\Delta\gamma^0_{\mathrm{VV}}$) is given by

$$\Delta\gamma^0_{\mathrm{VV}}(i,t) = \gamma^0_{\mathrm{VV}}(i,t) - \gamma^0_{\mathrm{VV}}(i,t_{\mathrm{pri}}) \tag{A3}$$

Vegetation causes significant cross-polarized backscatter that may obscure the snow-depth related signal. Consequently, a weighted combination of $\Delta\gamma^0_{\mathrm{VV}}$ and $\Delta\gamma^0_{\mathrm{CR}}$ is implemented using the forest cover fraction (FCF, bounded between 0 and 1):

$$\Delta\gamma^0(i,t) = (1 - FCF(i)) \cdot \Delta\gamma^0_{\mathrm{CR}}(i,t) + B \cdot FCF(i) \cdot \Delta\gamma^0_{\mathrm{VV}}(i,t) \tag{A4}$$

This weighted combination is parameterized by the second empirical fitting parameter B that controls the relative influence of the co-polarized backscatter change on the final snow depth retrievals. To remove outliers, we masked pixels in the result of (A4) with backscatter changes more than $+3$ dB and less than -3 dB.

A snow change index (SI, units of dB) captures changes in $\triangle\gamma^0$ over time, taking in information from multiple previous snow indexes and snow coverage data from the IMS. The algorithm is initiated with SI set to 0 for all pixels, and $SI = 0$ as long as the IMS dataset indicates no snow presence. Once snow presence is indicated, a previous snow index is calculated that takes the weighted average of the snow indexes centered around the last time step from the same orbital geometry (6 or 12 days ago) combined with the snow indexes from around that previous time step (+- 5 days or +- 11 days) (Equation A5) with weights that are the inverse distance in days between the previous time step and that image's acquisition date (Equation A6).

$$SI(i,t_{pri}) = \frac{1}{w} \sum_{t_{image}=t_{pri}-RI+1}^{t_{pri}+RI-1} w \times SI(i,t_{image}); RI \in 6,12,18,24[\text{days}] \tag{A5}$$

and w given by:

$$w = \begin{cases} [1..6..1] & RI = 6 \\ [1..12..1] & RI = 12 \\ [1..24..1] & RI = 24 \end{cases} \tag{A6}$$

For example, an image captured on January 30th in an orbital geometry that captures an image every 6 days ($RI = 6$) would multiply all the previously calculated snow indexes from January 19th to 29th (January 24th $\pm$ 5 days) by the repeat interval minus number of days separating each images from the previous image acquisition date (January 24th) so a vector of [1, 2, 3, 4, 5, 6, 5, 4, 3, 2, 1]. This sum would then be divided by that same vector with days without images removed to get the previous snow index.

The current time step's $\triangle\gamma^0$ is then added to this previous snow index to calculate the current snow index. If the currently calculated snow index is negative it is set to zero for this time step (Equation A7).

$$SI(i,t) = \begin{cases} \max(0, [SI(i,t_{pri}) + \triangle\gamma^0]) & IMS = \text{Snow} \\ 0 & IMS = \text{No Snow} \end{cases} \tag{A7}$$

Finally we convert the current snow index in dB to snow depth in meters by multiplying it by the parameter C (Equation A8). C controls the increase of snow depth correlated with increasing backscatter and was varied between 0 to 1 in increments of 0.01.

$$SD(i,t) = C * SI(i,t) \tag{A8}$$

A3 Wet snow flagging

Liquid water in snowpacks absorbs significant amounts of microwave energy, causing large backscatter decreases and potential issues with the snow depth retrieval algorithm. To reduce this potential source of error, a binary wet snow flag is applied

that attempts to identify changes in backscatter that result from wetting of the snow (causing a strong decrease) or refreezing (causing a strong increase) instead of changes in snow depth. The wet flag is also applied if SI drops below zero in a region where the IMS still indicates snow presence, which attempts to capture snow wetness in regions of shallow or patchy snow cover or highly vegetated areas. Since different orbit geometries have different local incidence angles and record data at different times of the day (06:00 and 18:00 LT), the wet snow flag is only calculated for changes between images of the same orbital geometry. Additionally, once a pixel has been flagged as wet it continues to be wet until a refreezing event occurs on that pixel.

For a pixel with less than 50% FCF if the cross polarized ratio drops by more than 2 dB from the previous image with the same orbital geometry we flag that pixel as wet snow. The same applies for a drop of more than 2 dB in the co-polarized backscatter for regions with greater than 50% FCF. This wet snow flag then continues forward for that orbital geometry until an increase of 1 dB in the cross-polarized ratio (for regions of FCF $<$ 50%) or co-polarized ratio (FCF $>$ 50%) is observed in the time series. After which that image and all subsequent images from that relative orbit geometry are flagged dry until the next drop in backscatter is observed (Equation A9).

$$
\text{Wet Flag}(i,t) =
\begin{cases}
\text{wet} & \triangle\gamma^0_{CR/VV}(i,t) < -2 \text{ dB} \\
\text{wet} & \text{Wet Flag}(i,t_{pri}) = \text{wet}; \triangle\gamma^0_{CR/VV}(i,t) < +1\text{dB} \\
\text{wet} & SI(i,t) < 0; IMS(i,t) = \text{Snow} \\
\text{dry} & t = \text{August 1st} \\
\text{dry} & \triangle\gamma^0_{CR/VV}(i,t) > +1 \text{ dB} \\
\text{dry} & \text{Wet Flag}(i,t_{pri}) = \text{dry}; \triangle\gamma^0_{CR/VV}(i,t) > -2 \text{ dB}
\end{cases}
\tag{A9}
$$

After February 1st, if a pixel was flagged as wet for 50% or more of the previous 4 observations from the same orbital geometry, we consider the snowpack to be permanently wet at that location and flag as wet the remainder of the time series until the next August 1st.

Appendix B: East River Basin case study

We also present a case study to evaluate the utility of the S1 algorithm for basin-wide snow depth analysis using spatially-distributed snow depth measurements over the East River Basin (ERB) in Colorado, USA. We selected this basin because of 1) its importance as a tributary of the Colorado River, which provides water to more than 40 million people, 2) its complex terrain and varying forest cover, and 3) the availability of additional snow datasets, including measurements from two SNOTEL stations, ASO lidar-derived snow depths, modeled snow depths from the iSnobal energy balance model, and a variety of additional measurements from in situ instrumentation associated with the Sublimation of Snow (SoS), Surface Atmosphere Integrated Field Laboratory (SAIL), and Supporting Advancement in Weather and Water Prediction in the Upper Colorado River Basin (SPLASH) campaigns.

440   We implemented the S1 algorithm over the ERB from 2016-2023 using the WUS-optimized parameters. We temporally interpolated gaps in S1-derived snow depths (typically resulting from wet-snow flagging) by assigning each missing pixel a value using the observation nearest in time. To compare the S1-derived snow depths with the variety of available data, we calculate the mean and interquartile range of all pixels within the study site for each available S1 image. We compare these basin-wide average snow depths to spatial averages of ASO lidar snow depths and iSnobal modeled snow depths, as well as
445   point measurements from the two SNOTEL stations.

For our ERB case study, we incorporated snow depth data from two SNOTEL stations (Schofield:737 and Butte:380), eight snow depth maps generated by ASO from airborne lidar data (Painter, 2018), and the physically based snow energy balance iSnobal model (Meyer et al., 2022).

Visual examination of S1 snow depth maps at 90 m resolution in the ERB (Figure B1) reveals high variability in snow
450   depth over sub-km length scales, likely reflecting the low signal to noise ratio of the radar data. Despite this variability, some realistic temporal patterns are discernible. Higher elevations appear to receive snow first and lose snow last, accumulating deeper snowpacks than lower elevations. Mean snow depth values over the basin agree well with snow depth recorded at the Schofield Pass SNOTEL station, especially during periods of high accumulation. This agreement supports our conclusion that this technique is best-suited to capturing winter patterns in snow accumulation at the basin scale. There is less agreement during
455   the spring and summer, which is expected due to increases the spatial extent of wet snow. Snow depths from two SNOTEL stations, ASO lidar measurements, and snow energy balance modelling generally remain within the interquartile region of snow depths measured with S1. Timing of peak snow depths at the two SNOTEL sites and from S1 agree strongly. Comparison with external snow depth data suggest that S1 can provide reasonable estimates of winter snow depth at the basin scale in mountainous areas where alternative sources of snow depth data may not be available. However, this technique does not appear
460   to reliably capture interannual variability in snow depth that may be of interest to water managers.

Appendix C: QSI Lidar validation at SNOTEL sites

The lidar snow depth data was validated against SNOTEL record. To minimize uncertainty in horizontal accuracy of points to pixels comparison, we created 3m buffer around snotel location and calculated summary statistics (mean and standard deviation) of lidar pixels within the buffer.

Table C1. SNOTEL and Lidar Data (2020)

Site	SNOTEL Value (m)	Mean Lidar Value (m)	Standard Deviation
Banner	1.47	1.49	0.024
Dry Creek	1.63	1.68	0.103
East River Fraser	1.75	1.77	0.072
Mores Creek	1.80	1.86	0.05
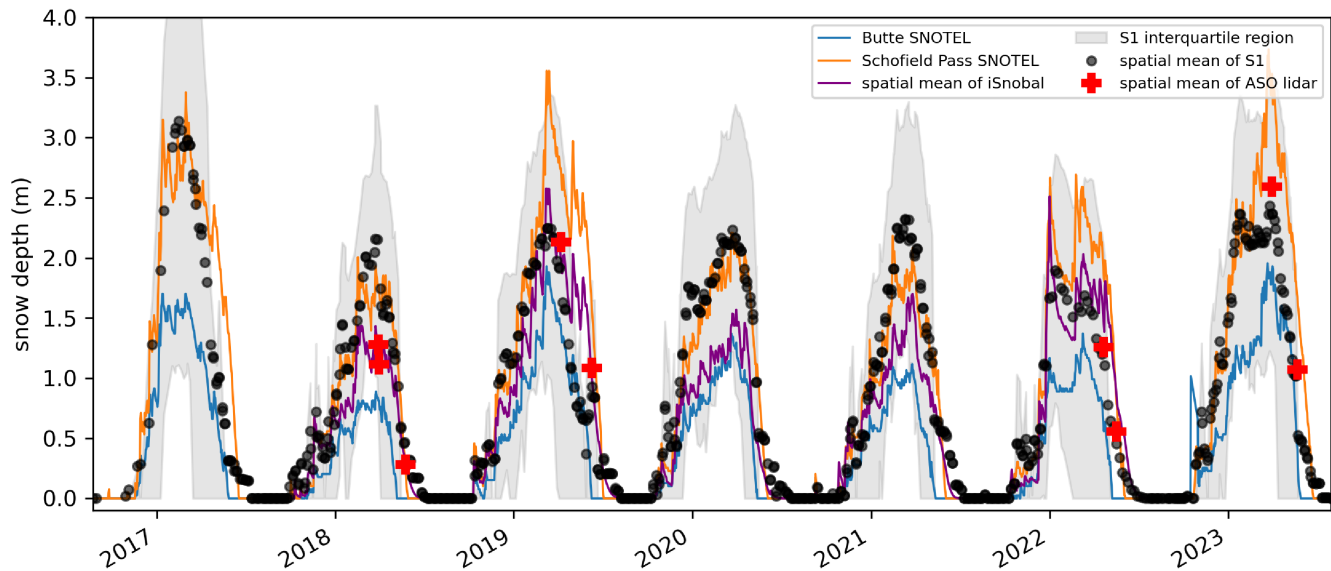
Figure B1. S1 snow depth time series for the East River Basin (see location in Figure 2). Mean snow depth across the catchment at each time step compared to snow depth data from two nearby SNOTEL stations, ASO lidar, and snow energy balance modelling.

Table C2. SNOTEL and Lidar Data (2021)

Site	SNOTEL Value (m)	Mean Lidar Value (m)	Standard Deviation
Banner	1.55	1.52	0.024
Cameroon	1.68	1.66	0.073
Fraser	1.51	1.54	0.071
Little Cottonwood	1.83	2.02	0.105
Mores Creek	1.88	1.89	0.038

465 **Appendix D: Parameter Optimization**

D1 Parameter Importance's

The optimal parameter values for our WUS validation dataset are $A = 1.5$, $B = 0.1$, and $C = 0.59$. Of these three parameters, changing C has the largest impact on RMSE ($\frac{\partial \text{RMSE}}{\partial A}$=0.207, $\frac{\partial \text{RMSE}}{\partial B}$=0.176, $\frac{\partial \text{RMSE}}{\partial C}$=0.908, Table D1). Because C is used as a scaling parameter in (1), it has no impact on R. Modifying B has a larger impact on scene-wide R values than does changing
470 A ($\frac{\partial R}{\partial A} = 0.035$, $\frac{\partial R}{\partial B} = 0.101$). However, when considering only pixels with FCF < 25%, changing A has a larger impact on R and RMSE. In contrast, B increases in importance for high FCF pixels.

We use the Banner 2021 validation dataset to further illustrate the sensitivity of the S1 snow depth retrievals to the three parameters (Figure D1a-c). Changes in the B and C parameter have approximately linear effects on the change in mean scene-
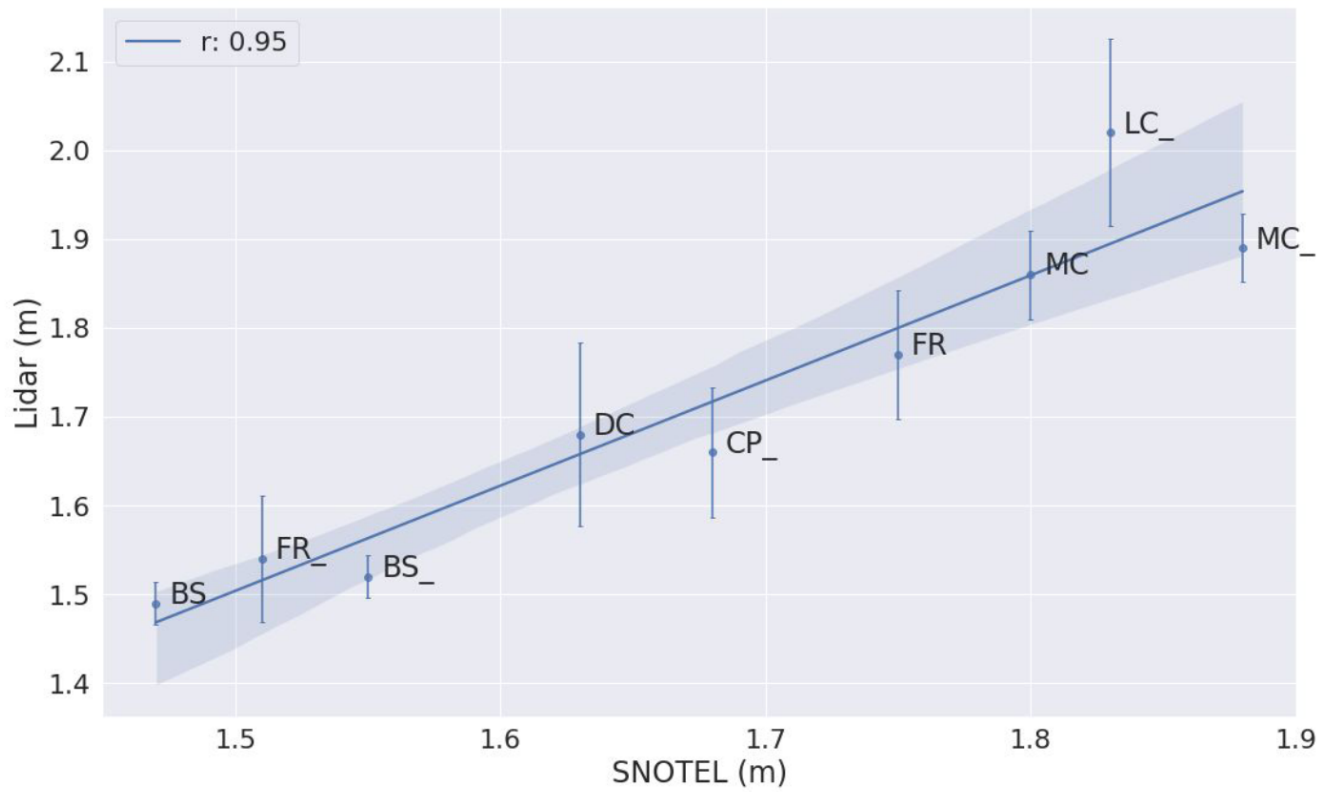
Figure C1. Comparison between the SNOTEL snow depth record against mean of lidar pixels within 3m of SNOTEL location.

Table D1: Parameter Sensitivity			
	All Pixels	**<25% FCF**	**>75% FCF**
$\partial\,\mathrm{RMSE}\,/\,\partial\,\mathrm{A}$	0.207	0.454	0.144
$\partial\,\mathrm{RMSE}\,/\,\partial\,\mathrm{B}$	0.176	0.019	0.367
$\partial\,\mathrm{RMSE}\,/\,\partial\,\mathrm{C}$	0.908	1.871	0.412
$\partial\,R\,/\,\partial\,\mathrm{A}$	0.035	0.047	0.030
$\partial\,R\,/\,\partial\,\mathrm{B}$	0.101	0.013	0.226
$\partial\,R\,/\,\partial\,\mathrm{C}$	0.000	0.000	0.000
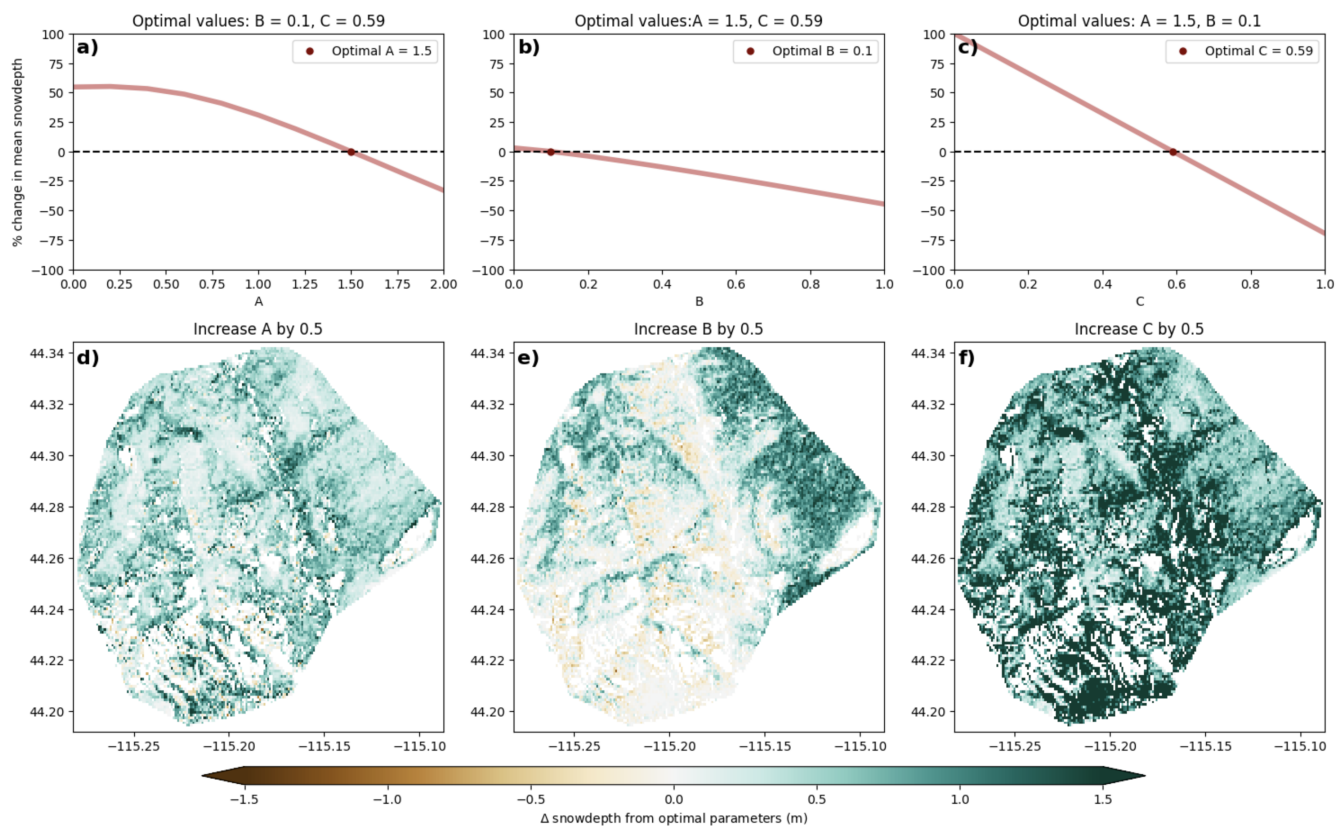
Figure D1. Percent change in scene-wide mean snow depth with varying A, B, and C parameters from optimized values (A = 1.5, B = 0.1, C = 0.59) for the Banner Summit 2021 site (a-c). Changes in S1 snow depth retrievals when increasing each parameter by 0.5 from the optimal value and keeping the other parameters at their optimal value (d-f).

wide snow depth, with changes to C impacting the snow depth retrieval the greatest. Changes in A were generally linear until
475 ≈0.5m where minimal snow depth changes were observed for further decreases in A. Increasing the A parameter primarily impacts higher elevation areas with lower FCF (Figure D1d), while increasing B results in increased snow depths in lower elevation forested regions and actually causes slight a snow depth decrease in the less forested regions (Figure D1e). Modifying the scaling parameter C affects all pixels, with the largest changes in regions with the greatest retrieved snow depths.

We found that the C parameter has the greatest impact on RMSE (Table D1) and total retrieved snow depth (Figure D1),
480 indicating that C is the most important parameter to optimize if minimizing scene-wide RMSE the primary consideration. Since C simply scales values in the final step of the retrieval, this parameter can be optimized efficiently and should be adjusted first when applying this technique at a new site.

The A and B parameters had a much lower impact on scene-wide RMSE but controlled the spatial and temporal distribution of error. As such, practitioners optimizing these two parameters should evaluate the environmental characteristics of areas with
485 high RMSE. Optimizing B may be most important in areas with greater forest cover, while conversely, optimizing A may

be more important in high-elevation areas with low forest cover. Importantly, A and B are not independent. Varying one will cause the other to be mis-optimized, highlighting a potential weakness of this empirical model. A potential avenue to lower RMSE across a scene with varied environmental characteristics could be to apply two implementations of the algorithm, one optimized for areas with dense forest cover and another optimized for alpine areas with sparse vegetation.

490   While we did not evaluate the impact of outliers on parameter optimization, visual examination of 2021 S1 snow depth results at the Banner study site shows isolated areas of extreme snow depth along a rugged ridgeline at the center of the site (Figure 5b). These extreme outliers in snow depth likely caused a decrease in C parameter to and a corresponding decrease in snow depths in other areas, potentially introducing a negative bias in the S1 snow depth results. These outliers are also visible in (Figure 4c) with some outliers over 4+ meters apparent in the S1 retrievals but no in the lidar. To mitigate this issue, it may

495   be advantageous to perform parameter optimization on a high-confidence subset of the radar data, within elevation bands, or after outlier removal.

Appendix E: Wet Snow Thresholds

The S1 algorithm has increased uncertainty over areas with wet snow (Lievens et al., 2022). Hence it is important to inspect how wet snow identification changes based on the wet snow parameters contained within the algorithm. As detailed in Section 2.3,

500   the wet snow parameters include the wet snow backscatter threshold, refrozen snow backscatter threshold, and the alt-wet flag that marks pixels with negative snow depth changes as wet. When attempting to optimize these parameters to minimize scene-wide RMSE, we found that no global optimum exists. Instead, we found that by increasing both the wet snow threshold and refrozen snow threshold, RMSE decreases at the expense of a reduced number of retrieved snow depths as more pixels are masked out. This tradeoff is visualized in Figure E1, with a more granular analysis in Figure E5 in Appendix B. Our selected

505   parameters of a wet snow threshold of -3 dB, a freezing threshold of +2 dB, and choosing to keep the alt-wet snow flag enabled provide a good compromise that results in an effective wet snow mask without overmasking to artificially boost algorithm performance.

We illustrate the efficacy of the wet snow mask again using the Banner 2021 dataset (Figure E2a, b) concurrently with snow depth and air temperature measurements from the Banner SNOTEL site (Figure E2c). During the beginning of the season,

510   there is a large spike in wet snow pixels corresponding with a warm, early season snow event and subsequent melt. From mid-December through late February we observe mostly dry snow across the scene, with the exception of some wet snow areas at lower elevations. In March we begin to observe large areas of wet snow corresponding with the onset of the snow melt season.

To explore the choice to use a freezing threshold of +1dB we have some more detailed visualization of the difference. These include: maps of flagged no snow, wet snow, and dry snow for the +1dB and +2dB for a freezing threshold (Figure

515   E3), time series of wet vs. dry pixel counts from the Banner study site and temperature and snow depth data from the Banner Summit SNOTEL (Figure E4), and plots of RMSE and fration of dry pixels for permutations of freeze threshold, new wet snow threshold, and the alternative wet flag (Figure E5).
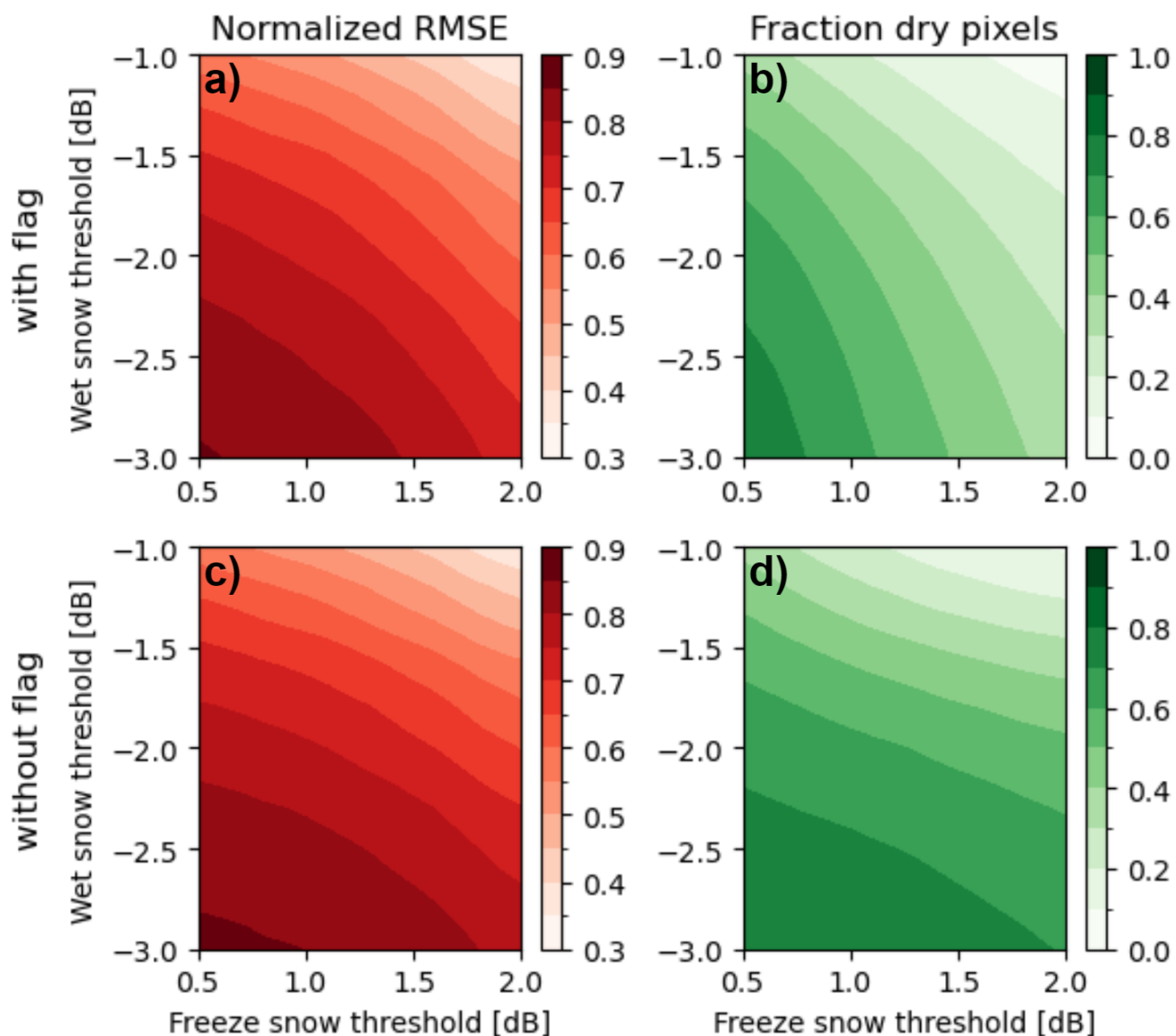
Figure E1. Binned mean normalized RMSEs (a & c) and fraction of dry pixels (b & d) for permutations of the newly wet and freezing thresholds and with (top row) and without (bottom row) the alternative wet snow flagging for the Banner 2021 lidar flight.
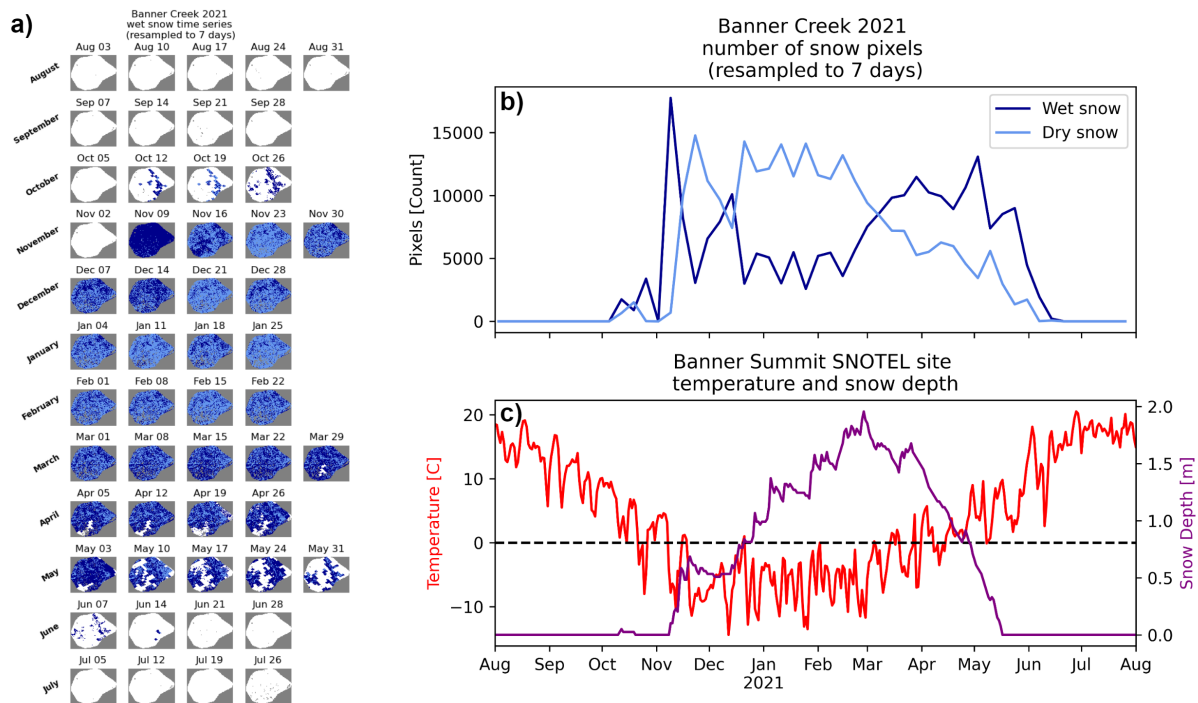
Figure E2. Time series of snow classifications for the 2020-2021 winter at the Banner study site (a) with no snow (white), dry snow (light blue), wet snow (dark blue). Number of dry vs. wet snow pixels in the scene from August 2020 to August 2021 (b), and temperature and snow depth values from the Banner Summit SNOTEL (c).

E1   Wet snow flagging parameters

The three wet snow parameters (wet snow flag, alt-wet snow flag, and refreeze flag) were not systematically optimized by Lievens et al. (2022). During our analysis we found the original refrozen snow threshold of +2dB to be overly conservative: pixels that we expect to refreeze remain wet throughout the entire winter season, despite air temperatures dropping well below freezing. We noted a jump in backscatter in these pixels, but not enough to satisfy the +2dB threshold. Similar considerable (but not quite +2dB) jumps in VV backscatter during refreezing events were also observed by Lund et al. (2022). The +1dB refrozen snow threshold we implemented resulted in a more realistic match with SNOTEL temperatures (Figure E2). A comparison of wet snow time series of Banner Creek using the original +2dB freeze snow threshold vs. our new +1dB freeze snow threshold can be seen in Figure E3 and Figure E4 in Appendix B.

With our optimized wet snow flagging parameters, the time series of wet snow and dry snow pixels matches well with the temperature and snow depth trends observed at the Banner Summit SNOTEL site (Figure E2). The spatial progression of melt agrees well with the SNOTEL temperature and snow depth measurements. Wet snow is observed in the early accumulation season (October through early December) when warmer daytime temperatures and mixed phase precipitation occur. Then, as
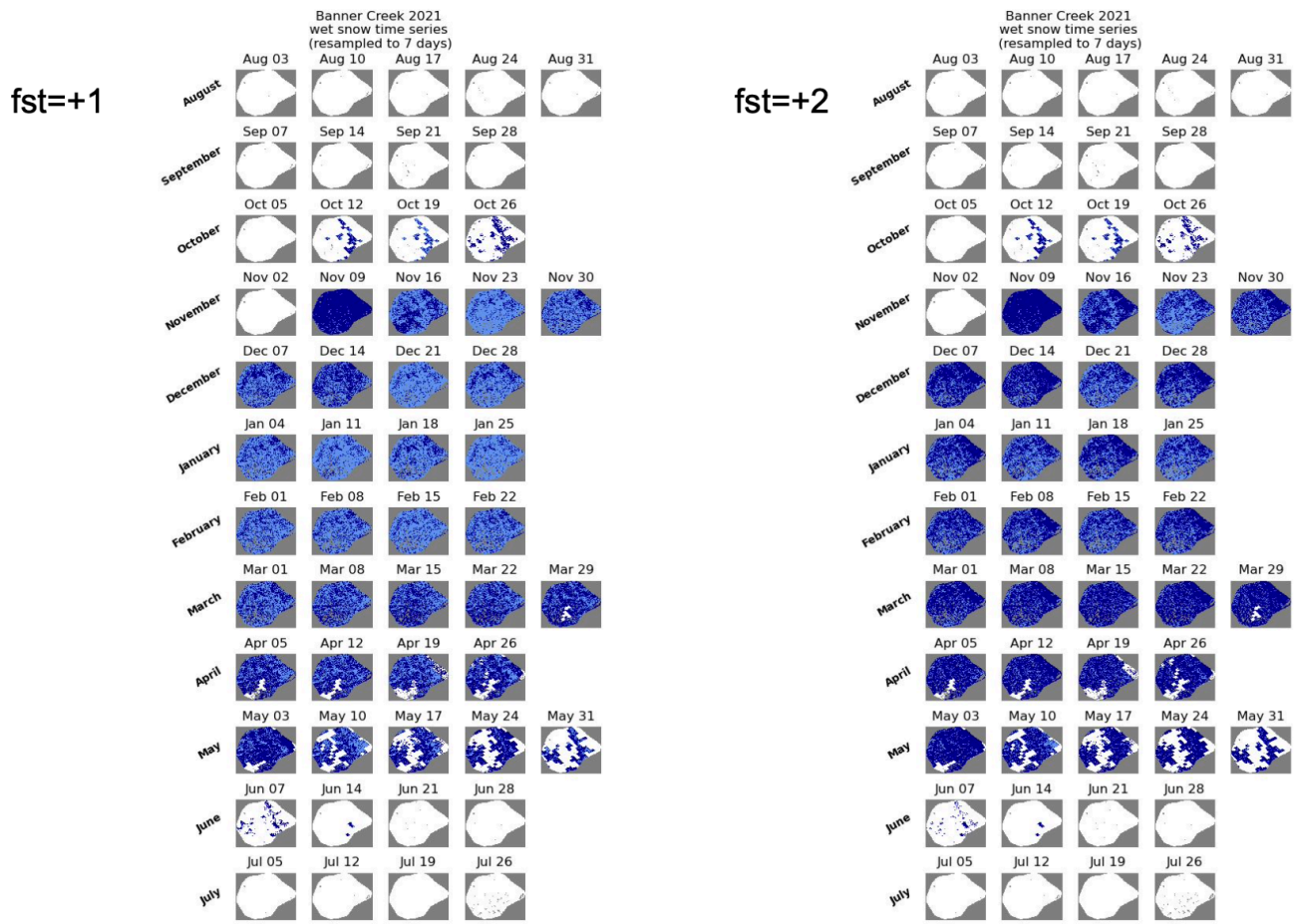
Figure E3. Maps of flagged wet snow (dark blue), dry snow (light blue), and no snow (white) for a +1dB freeze threshold (left) and +2dB freeze threshold (right).
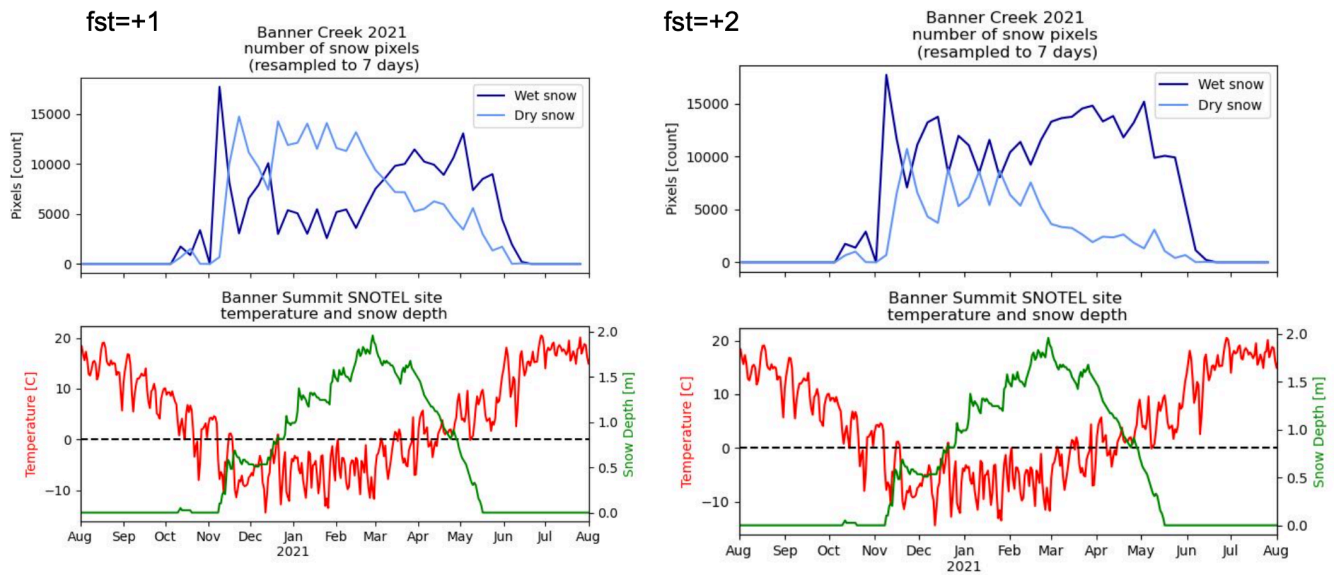
Figure E4. Time series of pixel counts for wet snow (dark blue) and dry snow (light blue) at the Banner study site for a +1dB freeze threshold (left) and +2dB freeze threshold (right) along with temporally matching temperature and snow depth data from the Banner Summit SNOTEL in the bottom row.

Banner Creek 2021
RMSE and fraction of dry pixels
vs. wet and freeze snow thresholds
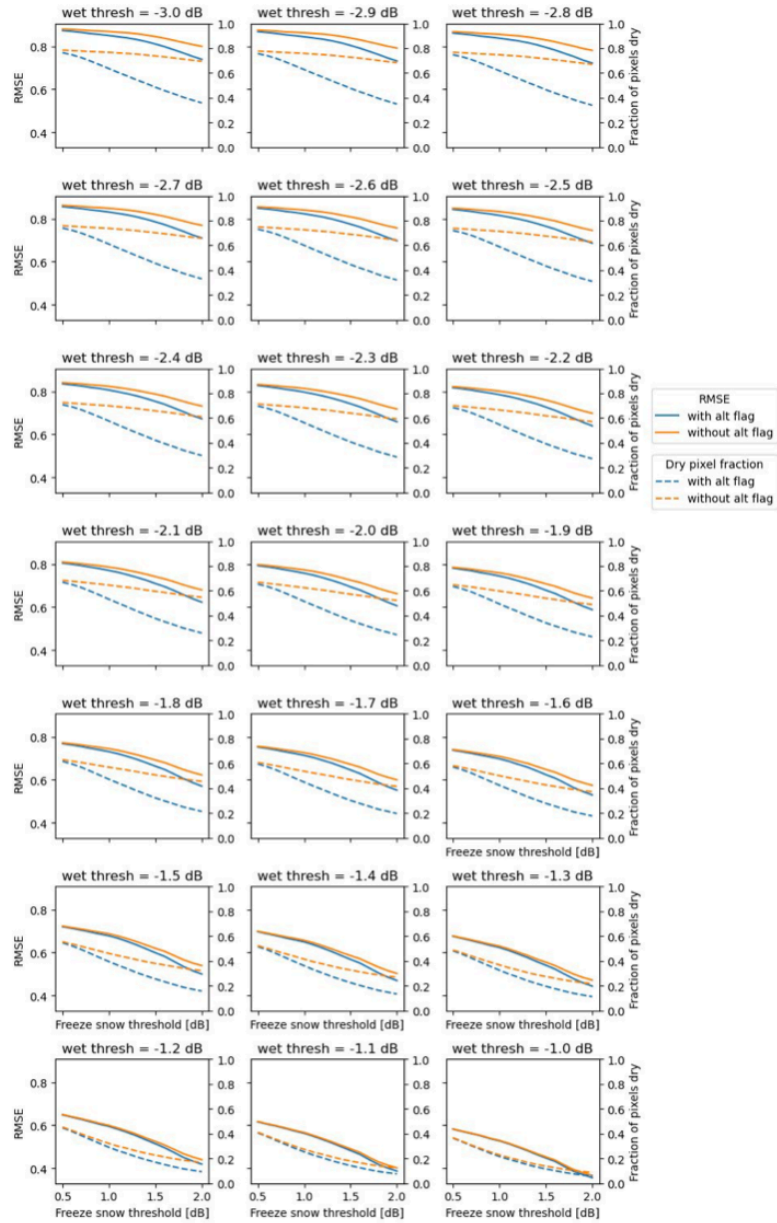
daytime temperatures progressively cool, water within the snowpack freezes and dry snow precipitation increases, expanding dry snow extent in the colder winter months (mid December through early March). Finally, warmer spring temperatures and increased shortwave radiation introduce surface melt in the snowpack, turning dry snow to wet snow beginning in mid-March until the snow melts away. This progression also coincides well with elevation: at Banner Creek, snow at lower elevations is more often observed as wet, and snow at higher elevations is more often observed as dry.

Though we make these recommendations for wet snow parameters, end users will have to make a final selection of parameter values that consider algorithm accuracy alongside the number of retrieved measurements. Additionally, it is important to remember that this is a tool intended for the accumulation season (Tsang et al., 2022). Though the pixels flagged as wet snow can often follow believable snow depth trends, we suggest caution in the use of these pixels, as changes in snow depth are likely not due to changes in volume scattering as prescribed in the algorithm. At the point that our algorithm flags a pixel as wet, it might be best to start considering other methods to continue tracking the snow depth and melt at that pixel, such as model output or optical-infrared imagery.

Author contributions. Conceptualization: ZH, HPM, QB, RP. Writing: ZH, RP, JT, QB, EG, DD, AM, RB, HPM Analysis: ZH, RP, GB, DD, EG, AM, NA, RB. Repository: ZH, RP, GB, EG. Funding Acquisition: HPM, CV. Planning: HPM, CV, KE. Editing: ZH, HPM, RP, JT

Competing interests. The authors report they have no competing interests.

Acknowledgements. We wish to thank Dr. Tate Meehan for his suggestion of repository name. Dr. Joe Meyer for sharing SnowModel data for the East River Basin. Emma Marshall for helping with implementing the algorithm using Xarray.

References

Abedisi, N., Marshall, H., Vuyovich, C., Elder, K., Hiemstra, C., and Durand, M.: SnowEx20-21 QSI Lidar Vegetation Height 0.5m UTM Grid, Version 1, NASA National Snow and Ice Data Center Distributed Active Archive Center., https://doi.org/10.5067/8rbiuipeuj7z, 2022.

Agency, E. S.: Copernicus Global Digital Elevation Model, https://doi.org/10.5270/esa-c5d3d65, 2021.

Bair, E. H., Stillinger, T., and Dozier, J.: Snow Property Inversion From Remote Sensing (SPIReS): A Generalized Multispectral Unmixing Approach With Examples From MODIS and Landsat 8 OLI, IEEE Transactions on Geoscience and Remote Sensing, 59, 7270–7284, https://doi.org/10.1109/tgrs.2020.3040328, 2021.

Bales, R. C., Molotch, N. P., Painter, T. H., Dettinger, M. D., Rice, R., and Dozier, J.: Mountain hydrology of the western United States, Water Resources Research, 42, https://doi.org/10.1029/2005wr004387, 2006.

Barnett, T. P., Adam, J. C., and Lettenmaier, D. P.: Potential impacts of a warming climate on water availability in snow-dominated regions, Nature, 438, 303–309, https://doi.org/10.1038/nature04141, 2005.

Bernier, M. and Fortin, J.-P.: The potential of times series of C-Band SAR data to monitor dry and shallow snow cover, IEEE Transactions on Geoscience and Remote Sensing, 36, 226–243, https://doi.org/10.1109/36.655332, 1998.

Bernier, M., Fortin, J., Gauthier, Y., Gauthier, R., Roy, R., and Vincent, P.: Determination of snow water equivalent using RADARSAT SAR data in eastern Canada, Hydrological Processes, 13, 3041–3051, https://doi.org/10.1002/(sici)1099-1085(19991230)13:18<3041::aid-hyp14>3.0.co;2-e, 1999.

Brangers, I., Marshall, H.-P., Lannoy, G. J. M. D., and Lievens, H.: Tower based C-band measurements of an alpine snowpack, EGU General Assembly 2023, https://doi.org/10.5194/egusphere-egu23-17234, 2023.

Buchhorn, M., Lesiv, M., Tsendbazar, N. E., Herold, M., Bertels, L., and Smets, B.: Copernicus Global Land Cover Layers-Collection 2, Remote Sensing, 108, https://doi.org/10.3390/rs12061044, 2020.

Bühler, Y., Adams, M. S., Bösch, R., and Stoffel, A.: Mapping snow depth in alpine terrain with unmanned aerial systems (UASs): potential and limitations, The Cryosphere, 10, 1075–1088, https://doi.org/10.5194/tc-10-1075-2016, 2016.

Chang, W., Tan, S., Lemmetyinen, J., Tsang, L., Xu, X., and Yueh, S. H.: Dense Media Radiative Transfer Applied to SnowScat and SnowSAR, IEEE Journal of Selected Topics in Applied Earth Observations and Remote Sensing, 7, 3811–3825, https://doi.org/10.1109/jstars.2014.2343519, 2014.

Currier, W. R., Pflug, J., Mazzotti, G., Jonas, T., Deems, J. S., Bormann, K. J., Painter, T. H., Hiemstra, C. A., Gelvin, A., Uhlmann, Z., Spaete, L., Glenn, N. F., and Lundquist, J. D.: Comparing Aerial Lidar Observations With Terrestrial Lidar and Snow-Probe Transects From NASA's 2017 SnowEx Campaign, Water Resources Research, 55, 6285–6294, https://doi.org/10.1029/2018wr024533, 2019.

Deems, J. S., Painter, T. H., and Finnegan, D. C.: Lidar measurement of snow depth: a review, Journal of Glaciology, 59, 467–479, https://doi.org/10.3189/2013jog12j154, 2013.

Deschamps-Berger, C., Gascoin, S., Shean, D., Besso, H., Guiot, A., and López-Moreno, J. I.: Evaluation of snow depth retrievals from ICESat-2 using airborne laser-scanning data, The Cryosphere, 17, 2779–2792, https://doi.org/10.5194/tc-17-2779-2023, 2023.

Ding, K.-H., Xu, X., and Tsang, L.: Electromagnetic Scattering by Bicontinuous Random Microstructures with Discrete Permittivities, IEEE Transactions on Geoscience and Remote Sensing, 48, 3139–3151, https://doi.org/10.1109/tgrs.2010.2043953, 2010.

Dressler, K. A., Leavesley, G. H., Bales, R. C., and Fassnacht, S. R.: Evaluation of gridded snow water equivalent and satellite snow cover products for mountain basins in a hydrologic model, Hydrological Processes, 20, 673–688, https://doi.org/10.1002/hyp.6130, 2006.

585   Enderlin, E. M., Elkin, C. M., Gendreau, M., Marshall, H., O'Neel, S., McNeil, C., Florentine, C., and Sass, L.: Uncertainty of ICESat-2 ATL06- and ATL08-derived snow depths for glacierized and vegetated mountain regions, Remote Sensing of Environment, 283, 113 307, https://doi.org/10.1016/j.rse.2022.113307, 2022.

Frerebeau, N., Lebrun, B., and Paradol, G.: gamma: Dose Rate Estimation from in-Situ Gamma-Ray Spectrometry, https://doi.org/10.5281/zenodo.2652393, r package version 1.0.4, 2023.

590   Fuller, M. C., Geldsetzer, T., and Yackel, J. J.: Surface-Based Polarimetric C-Band Microwave Scatterometer Measurements of Snow During a Chinook Event, IEEE Transactions on Geoscience and Remote Sensing, 47, 1766–1776, https://doi.org/10.1109/tgrs.2008.2006684, 2009.

Fuster, B., Sánchez-Zapero, J., Camacho, F., García-Santos, V., Verger, A., Lacaze, R., Weiss, M., Baret, F., and Smets, B.: Quality Assessment of PROBA-V LAI, fAPAR and fCOVER Collection 300 m Products of Copernicus Global Land Service, Remote Sensing, 12, 1017,
595   https://doi.org/10.3390/rs12061017, 2020.

Gagliano, E., Shean, D., Henderson, S., and Vanderwilt, S.: Capturing the Onset of Mountain Snowmelt Runoff Using Satellite Synthetic Aperture Radar, Geophysical Research Letters, 50, https://doi.org/10.1029/2023gl105303, 2023.

Hogenson, K., Kristenson, H., Kennedy, J., Johnston, A., Rine, J., Logan, T., Zhu, J., Williams, F., Herrmann, J., Smale, J., and Meyer, F.: Hybrid Pluggable Processing Pipeline (HyP3): A cloud-native infrastructure for generic processing of SAR data, 2020.

600   Homer, C., Dewitz, J., Jin, S., Xian, G., Costello, C., Danielson, P., Gass, L., Funk, M., Wickham, J., Stehman, S., Auch, R., and Riitters, K.: Conterminous United States land cover change patterns 2001–2016 from the 2016 National Land Cover Database, ISPRS Journal of Photogrammetry and Remote Sensing, 162, 184–199, https://doi.org/10.1016/j.isprsjprs.2020.02.019, 2020.

Hoppinen, Z., Brencher, G., and Palomaki, R.: Spicy Snow (Version 0.1.0) [Computer software]., https://doi.org/10.5281/zenodo.7946534, 2023.

605   Kelly, R. E. J. and Chang, A. T. C.: Development of a passive microwave global snow depth retrieval algorithm for Special Sensor Microwave Imager (SSM/I) and Advanced Microwave Scanning Radiometer-EOS (AMSR-E) data, Radio Science, 38, n/a–n/a, https://doi.org/10.1029/2002rs002648, 2003.

Kendra, J. R.: Microwave remote sensing of snow : an empirical/theoretical scattering model for dense random media, The University of Michigan Dissertation, 1995.

610   Lebrun, B., Frerebeau, N., Paradol, G., Guérin, G., Mercier, N., Tribolo, C., Lahaye, C., and Rizza, M.: gamma: An R Package for Dose Rate Estimation from In-Situ Gamma-Ray Spectrometry Measurements, Ancient TL, 38, 1–5, 2020.

Li, D., Wrzesien, M. L., Durand, M., Adam, J., and Lettenmaier, D. P.: How much runoff originates as snow in the western United States, and how will that change in the future?, Geophysical Research Letters, 44, 6163–6172, https://doi.org/10.1002/2017gl073551, 2017.

Lievens, H., Demuzere, M., Marshall, H.-P., Reichle, R. H., Brucker, L., Brangers, I., Rosnay, P. d., Dumont, M., Girotto, M., Immerzeel,
615   W. W., Jonas, T., Kim, E. J., Koch, I., Marty, C., Saloranta, T., Schöber, J., and Lannoy, G. J. M. D.: Snow depth variability in the Northern Hemisphere mountains observed from space, Nature Communications, 10, 4629, https://doi.org/10.1038/s41467-019-12566-y, 2019.

Lievens, H., Brangers, I., Marshall, H.-P., Jonas, T., Olefs, M., and Lannoy, G. D.: Sentinel-1 snow depth retrieval at sub-kilometer resolution over the European Alps, The Cryosphere, 16, 159–177, https://doi.org/10.5194/tc-16-159-2022, 2022.

Lund, J., Forster, R. R., Deeb, E. J., Liston, G. E., Skiles, S. M., and Marshall, H.-P.: Interpreting Sentinel-1 SAR Backscatter Signals
620   of Snowpack Surface Melt/Freeze, Warming, and Ripening, through Field Measurements and Physically-Based SnowModel, Remote Sensing, 14, 4002, https://doi.org/10.3390/rs14164002, 2022.

Mankin, J. S., Viviroli, D., Singh, D., Hoekstra, A. Y., and Diffenbaugh, N. S.: The potential for snow to supply human water demand in the present and future, Environmental Research Letters, 10, 114 016, https://doi.org/10.1088/1748-9326/10/11/114016, 2015.

Marshall, H., Deeb, E., Forster, R., Vuyovich, C., Elder, K., Hiemstra, C., and Lund, J.: L-Band InSAR Snow Depth Retrievals from Grand Mesa in NASA SnowEX 2020 Campaign, Institute of Electrical and Electronics Engineers, 2021.

McGrath, D., Webb, R., Shean, D., Bonnell, R., Marshall, H., Painter, T. H., Molotch, N. P., Elder, K., Hiemstra, C., and Brucker, L.: Spatially Extensive Ground-Penetrating Radar Snow Depth Observations During NASA's 2017 SnowEx Campaign: Comparison With In Situ, Airborne, and Satellite Observations, Water Resources Research, 55, 10 026–10 036, https://doi.org/10.1029/2019wr024907, 2019.

Meyer, J., Horel, J., Kormos, P., Hedrick, A., Trujillo, E., and Skiles, S. M.: Operational water forecast ability of the HRRR-iSnobal combination: an evaluation to adapt into production environments, Geoscientific Model Development, 16, 233–250, https://doi.org/10.5194/gmd-16-233-2023, 2022.

Miller, Z. S., Peitzsch, E. H., Sproles, E. A., Birkeland, K. W., and Palomaki, R. T.: Assessing the seasonal evolution of snow depth spatial variability and scaling in complex mountain terrain, The Cryosphere, 16, 4907–4930, https://doi.org/10.5194/tc-16-4907-2022, 2022.

Mätzler, C.: Applications of the interaction of microwaves with the natural snow cover, Remote Sensing Reviews, 2, 259–387, https://doi.org/10.1080/02757258709532086, 1987.

Naderpour, R., Schwank, M., Houtz, D., Werner, C., and Mätzler, C.: Wideband Backscattering From Alpine Snow Cover: A Full-Season Study, IEEE Transactions on Geoscience and Remote Sensing, 60, 1–15, https://doi.org/10.1109/tgrs.2021.3112772, 2022.

Nolan, M., Larsen, C., and Sturm, M.: Mapping snow depth from manned aircraft on landscape scales at centimeter resolution using structure-from-motion photogrammetry, The Cryosphere, 9, 1445–1463, https://doi.org/10.5194/tc-9-1445-2015, 2015.

NSIDC: IMS Daily Northern Hemisphere Snow and Ice Analysis at 1 km, 4 km, and 24 km Resolutions, Version 1 [Data Set], National Snow and Ice Data Center, https://doi.org/10.7265/n52r3pmc, 2008.

Painter: ASO L4 Lidar Snow Depth 50m UTM Grid, Version 1, https://nsidc.org/data/ASO_50M_SD/versions/1, 2018.

Painter, T. H., Berisford, D. F., Boardman, J. W., Bormann, K. J., Deems, J. S., Gehrke, F., Hedrick, A., Joyce, M., Laidlaw, R., Marks, D., Mattmann, C., McGurk, B., Ramirez, P., Richardson, M., Skiles, S. M., Seidel, F. C., and Winstral, A.: The Airborne Snow Observatory: Fusion of scanning lidar, imaging spectrometer, and physically-based modeling for mapping snow water equivalent and snow albedo, Remote Sensing of Environment, 184, 139–152, https://doi.org/10.1016/j.rse.2016.06.018, 2016.

Rittger, K., Raleigh, M. S., Dozier, J., Hill, A. F., Lutz, J. A., and Painter, T. H.: Canopy Adjustment and Improved Cloud Detection for Remotely Sensed Snow Cover Mapping, Water Resources Research, 56, https://doi.org/10.1029/2019wr024914, 2020.

Rosen, P. A., Hensley, S., Joughin, I. R., Li, F. K., Madsen, S. N., RodrÍgues, E., Goldstein, R. M., Bamler, R., and Hartl, P.: Synthetic aperture radar interferometry, Proceedings of the IEEE, 88, 333–382, https://doi.org/10.1088/0266-5611/14/4/001, 2000.

Rott, H., Malnes, E., Nagler, T., Pulliainen, J., Rebhan, H., Thompson, A., Yueh, S. H., Cline, D. W., Duguay, C., Essery, R., Haas, C., Heliere, F., Kern, M., and Macelloni, G.: Cold Regions Hydrology High-Resolution Observatory for Snow and Cold Land Processes, Proceedings of the IEEE, 98, 752–765, https://doi.org/10.1109/jproc.2009.2038947, 2010.

Ruiz, J. J., Lemmetyinen, J., Kontu, A., Tarvainen, R., Vehmas, R., Pulliainen, J., and Praks, J.: Investigation of Environmental Effects on Coherence Loss in SAR Interferometry for Snow Water Equivalent Retrieval, IEEE Transactions on Geoscience and Remote Sensing, 60, 1–15, https://doi.org/10.1109/tgrs.2022.3223760, 2022.

Schaefer, G. L. and Paetzold, R. F.: SNOTEL (SNOwpack TELemetry) And SCAN (Soil Climate Analysis Network), Automated Weather Stations for Applications in Agriculture and Water Resources Management: Current Use and Future Perspectives, 2000.

Schneider, D. and Molotch, N. P.: Real-time estimation of snow water equivalent in the Upper Colorado River Basin using MODIS-based SWE Reconstructions and SNOTEL data, Water Resources Research, 52, 7892–7910, https://doi.org/10.1002/2016wr019067, 2016.

Sciences, N. A. o.: Thriving on Our Changing Planet: A Decadal Strategy for Earth Observation from Space, The National Academies Press, https://doi.org/10.17226/24938, 2018.

Shaw, T. E., Gascoin, S., Mendoza, P. A., Pellicciotti, F., and McPhee, J.: Snow Depth Patterns in a High Mountain Andean Catchment from Satellite Optical Tristereoscopic Remote Sensing, Water Resources Research, 56, https://doi.org/10.1029/2019wr024880, 2020.

Shi, J. and Dozier, J.: Estimation of snow water equivalence using SIR-C/X-SAR. I. Inferring snow density and subsurface properties, IEEE Transactions on Geoscience and Remote Sensing, 38, 2465–2474, https://doi.org/10.1109/36.885195, 2000.

Smith, T. and Bookhagen, B.: Changes in seasonal snow water equivalent distribution in High Mountain Asia (1987 to 2009), Science Advances, 4, e1701 550, https://doi.org/10.1126/sciadv.1701550, 2018.

Stillinger, T., Rittger, K., Raleigh, M. S., Michell, A., Davis, R. E., and Bair, E. H.: Landsat, MODIS, and VIIRS snow cover mapping algorithm performance as validated by airborne lidar datasets, The Cryosphere, 17, 567–590, https://doi.org/10.5194/tc-17-567-2023, 2022.

Strozzi, T., Wiesmann, A., and Mätzler, C.: Active microwave signatures of snow covers at 5.3 and 35 GHz, Radio Science, 32, 479–495, https://doi.org/10.1029/96rs03777, 1997.

Sturm, M., Holmgren, J., and Liston, G. E.: A Seasonal Snow Cover Classification System for Local to Global Applications, Journal of Climate, 8, 1261–1283, https://doi.org/10.1175/1520-0442(1995)008<1261:assccs>2.0.co;2, 1995.

Sturm, M., Taras, B., Liston, G. E., Derksen, C., Jonas, T., and Lea, J.: Estimating Snow Water Equivalent Using Snow Depth Data and Climate Classes, Journal of Hydrometeorology, 11, 1380–1394, https://doi.org/10.1175/2010jhm1202.1, 2010.

Sturm, M., Goldstein, M. A., and Parr, C.: Water and life from snow: A trillion dollar science question, Water Resources Research, 53, 3534–3544, https://doi.org/10.1002/2017wr020840, 2017.

Sun, S., Che, T., Wang, J., Li, H., Hao, X., Wang, Z., and Wang, J.: Estimation and Analysis of Snow Water Equivalents Based on C-Band SAR Data and Field Measurements, Arctic, Antarctic, and Alpine Research, 47, 313–326, https://doi.org/10.1657/aaar00c-13-135, 2015.

Takala, M., Luojus, K., Pulliainen, J., Derksen, C., Lemmetyinen, J., Kärnä, J.-P., Koskinen, J., and Bojkov, B.: Estimating northern hemisphere snow water equivalent for climate research through assimilation of space-borne radiometer data and ground-based measurements, Remote Sensing of Environment, 115, 3517–3529, https://doi.org/10.1016/j.rse.2011.08.014, 2011.

Tarricone, J., Webb, R. W., Marshall, H.-P., Nolin, A. W., and Meyer, F. J.: Estimating snow accumulation and ablation with L-band InSAR, The Cryosphere Discussions, 2022, 1–33, https://doi.org/10.5194/tc-2022-224, 2022.

Tedesco, M. and Narvekar, P. S.: Assessment of the NASA AMSR-E SWE Product, IEEE Journal of Selected Topics in Applied Earth Observations and Remote Sensing, 3, 141–159, https://doi.org/10.1109/jstars.2010.2040462, 2010.

Tong, J., Déry, S. J., Jackson, P. L., and Derksen, C.: Testing snow water equivalent retrieval algorithms for passive microwave remote sensing in an alpine watershed of western Canada, Canadian Journal of Remote Sensing, 36, S74–S86, https://doi.org/10.5589/m10-009, 2010.

Tsai, Y.-L. S., Dietz, A., Oppelt, N., and Kuenzer, C.: Remote Sensing of Snow Cover Using Spaceborne SAR: A Review, Remote Sensing, 11, 1456, https://doi.org/10.3390/rs11121456, 2019.

Tsang, L., Durand, M., Derksen, C., Barros, A. P., Kang, D.-H., Lievens, H., Marshall, H.-P., Zhu, J., Johnson, J., King, J., Lemmetyinen, J., Sandells, M., Rutter, N., Siqueira, P., Nolin, A., Osmanoglu, B., Vuyovich, C., Kim, E. J., Taylor, D., Merkouriadi, I., Brucker, L., Navari, M., Dumont, M., Kelly, R., Kim, R. S., Liao, T.-H., and Xu, X.: Review Article: Global Monitoring of Snow Water Equivalent using High Frequency Radar Remote Sensing, The Cryosphere Discussions, 2021, 1–57, https://doi.org/10.5194/tc-2021-295, 2021.

Tsang, L., Durand, M., Derksen, C., Barros, A. P., Kang, D.-H., Lievens, H., Marshall, H.-P., Zhu, J., Johnson, J., King, J., Lemmetyinen, J., Sandells, M., Rutter, N., Siqueira, P., Nolin, A., Osmanoglu, B., Vuyovich, C., Kim, E., Taylor, D., Merkouriadi, I., Brucker, L., Navari, M., Dumont, M., Kelly, R., Kim, R. S., Liao, T.-H., Borah, F., and Xu, X.: Review article: Global monitoring of snow water equivalent using high-frequency radar remote sensing, The Cryosphere, 16, 3531–3573, https://doi.org/10.5194/tc-16-3531-2022, 2022.

Vreugdenhil, M., Navacchi, C., Bauer-Marschallinger, B., Hahn, S., Steele-Dunne, S., Pfeil, I., Dorigo, W., and Wagner, W.: Sentinel-1 Cross Ratio and Vegetation Optical Depth: A Comparison over Europe, Remote Sensing, 12, 3404, https://doi.org/10.3390/rs12203404, 2020.

Webster, R. and Oliver, M. A.: Geostatistics for Environmental Scientists, vol. 1, John Wiley & Sons Ltd, The Atrium, Southern Gate, Chichester, West Sussex PO19 8SQ, England, 2 edn., ISBN 978-0-470-02858-2, https://doi.org/10.1002/9780470517277, 2007.

Wegmüller, U.: The effect of freezing and thawing on the microwave signatures of bare soil, Remote Sensing of Environment, 33, 123–135, https://doi.org/10.1016/0034-4257(90)90038-n, 1990.

West, R. D.: Potential applications of 1–5 GHz radar backscatter measurements of seasonal land snow cover, Radio Science, 35, 967–981, https://doi.org/10.1029/1999rs002257, 2000.

Zhu, J., Tsang, L., and Xu, X.: Modeling of Scattering by Dense Random Media Consisting of Particle Clusters With DMRT Bicontinuous, IEEE Transactions on Antennas and Propagation, 71, 3611–3619, https://doi.org/10.1109/tap.2023.3240562, 2023.